1. Introduction

Most of the Japanese breakwaters are of a composite type with heavy caissons resting on rubble rock foundations as shown in **Figure 1**. Expert divers rearrange rubble rocks and prepare a smooth contacting surface to avoid concentrated forces acting on the bottom slab of a caisson. We call such a surface a "smooth surface". On the other hand, a "rough surface" normally exists in the areas where a caisson does not rest on the foundation. The Ministry of Land, Infrastructure and Transport (MLIT) of Japan now prepares for proposing to employ a rougher surface instead of a "smooth surface" to shorten construction periods and reduce the associated costs.

However, it is suspected that an increase in the surface roughness might increase the moment on the bottom slab of the caisson that would affect the caisson design (Miyata et al. 1999), see **Figure 2**. However, to date there is no experimental data or information on how a caisson is actually supported by rubble rocks of even a "smooth surface" foundation. According to the Japanese Technical Standards for Port and Harbour Facilities (1983), the bottom slab of a caisson is assumed to be subject to a linearly distributed reaction force from the foundation. However, in reality, the foundation consists of discrete rubble rocks and that will generate concentrated contact forces between the caisson and foundation. At present no comprehensive study exists that has examined the effects of the surface roughness on the force support systems within rubble rock foundations. Therefore, a more basic study on force support systems of particulate media is required for a better understanding of the support systems generated by rubble rock foundations.

Discrete Element Methods (DEMs) are a family of numerical simulation methods for simulating the dynamic and pseudo static motions of a system of interacting rigid bodies (particles). In order to investigate force support systems of particulate media like rubble rocks as described above, the DEM has been chosen because it is capable of accessing particle-particle contact forces and contact forces between a particle and a plate.

The current report describes the general theory of DEM and mathematical development of the two-dimensional DEM with superquadric shaped particles and the three-dimensional DEM with ellipsoidal particles for analyzing systems of general shaped rigid particles. We investigate the force support systems of particulate media by using these two DEMs for a preliminary study concerning the support systems of a rubble rock foundation subjected to external loadings. In the DEM simulations, rubble rocks are modeled by smooth frictional particles. The rocks are then subject to a vertical loading of the weight of a caisson. DEM simulations performed in this report are: a) uniaxial compression tests of particulate media using the superquadric DEM, and b) similar tests using the ellipsoidal DEM. In this report, we give some preliminary observations and discussions on the force support systems of particulate media.

2. Discrete Element Method (DEM)

This chapter provides a literature survey on the developments of Discrete Element Methods and its mathematical descriptions. In section 2.1, the literature survey is provided. In section 2.2, the general theory for two-dimensional circular shaped DEM, which is most

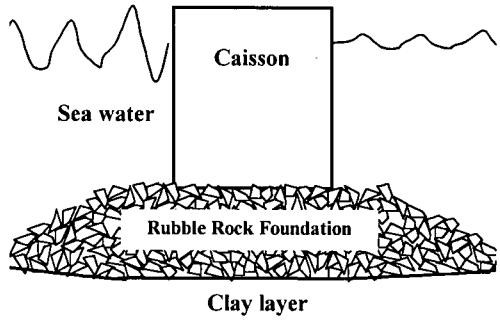

Figure 1 Cross section of a composite type

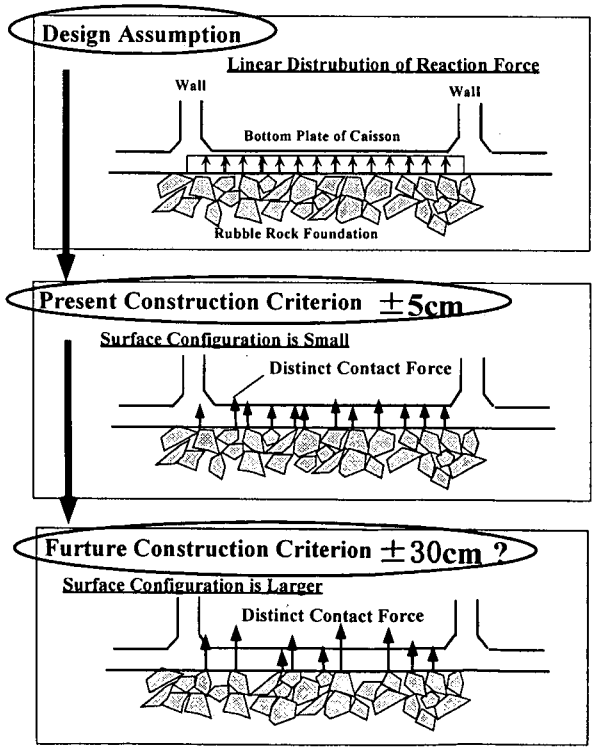

Figure 2 Schematic view of force support systems of a rubble rock foundation

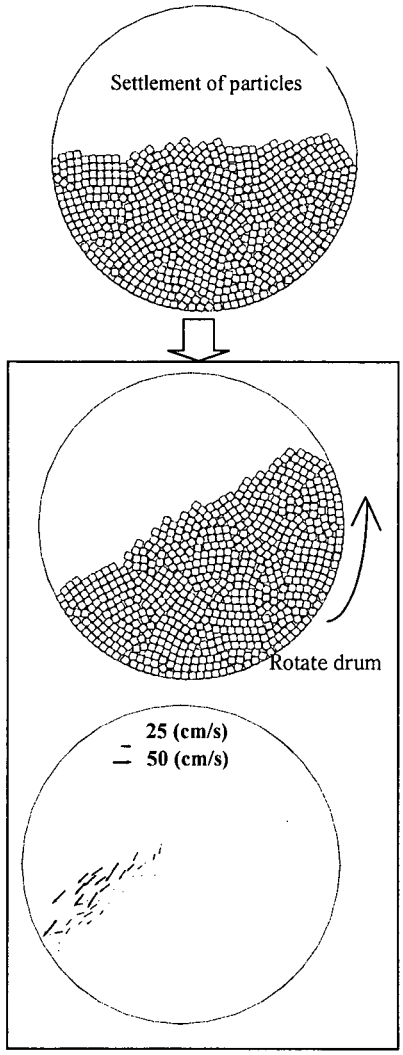

Figure 3 Example of DEM simulation

commonly used, is described. In sections 2.3 and 2.4, we describe the mathematical developments for two advanced DEMs, which employ an analytical particle shape representation. These two DEMs are a two-dimensional superquadric particle DEM and three-dimensional ellipsoidal DEM.

2.1 Literature Survey

(1) Introduction

Discrete Element Methods (DEMs) are a family of numerical simulation methods for simulating the dynamic and pseudo static motions of a system of interacting rigid bodies. **Figure 3** shows a schematic picture of simulation process by DEM (Mustoe and Miyata, 2001). In this simulation, material flow of particles in a rotating drum is simulated. As shown in the figure, DEMs are capable of accessing accelerations, velocities, displacements of particles and interacting forces between particles in both dynamic and pseudo

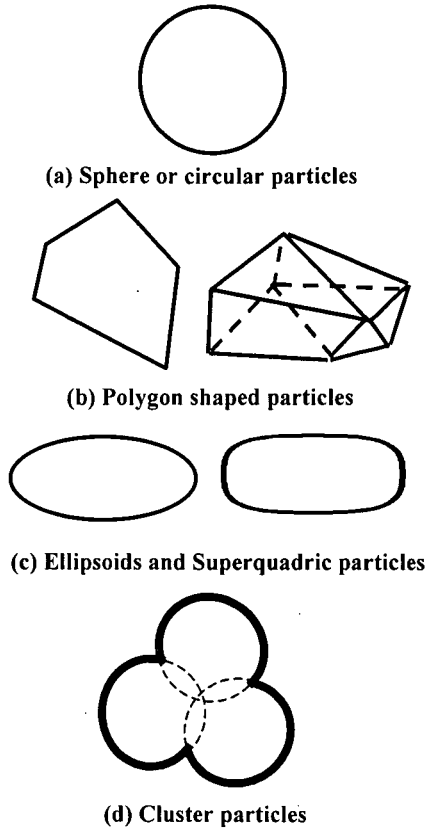

Figure 4 Particle shapes for DEM

static conditions. Compared with Finite Element Methods, which are based on a continuum mechanics, DEMs have the advantage to predict particulate level information as described above.

An early computational method similar to modern DEMs was originally introduced by Alder and Wainwright (1956) to study molecular dynamics. Note, DEMs were first developed to study stability of jointed arbitrary shaped rock-masses, see Cundall (1971). Subsequent DEMs have been developed and used to solve a wide range of engineering problems, involving the mechanical analysis of a system of interacting bodies, see two special conference proceedings and a special volume: "*Proceedings of the 1st U.S. Conference on Discrete Element Methods*, Mustoe et al eds.(1989) ", "Proceedings of the 2nd International Conference on Discrete Element Methods, Williams and Mustoe eds.(1993)", and "Special Issue of J. Powder Technology (Seville et al. editors (2000)). "

(2) Shape representations of particle

In many DEMs cylindrical or spherical shaped particles are usually employed because of the efficiency afforded by the simple contact detection as shown in **Figure 4(a)**. However, in some physical situations, more sophisticated DEM-based numerical models are

required, which account for the shape and size distributions of the system of bodies. A number of DEMs for non-circular shaped bodies have been recently developed and applied to different types of engineering analyses. DEMs for general shaped bodies may be categorized as follows: i) polygon shaped bodies (**Figure 4(b)**), ii) algebraically defined surface functions such as ellipsoids or superquadrics (Barr (1981)) that define any point on the surface of the body (**Figure 4(c)**), iii) clusters of rigidly or elastically connected overlapping cylindrical or spherical bodies (**Figure 4(d)**),.

Alternative DEMs with circular body geometry have attempted to account for particle shape by inhibiting or limiting the particle rotation. For example, Ting and Corkum (1988), increased the polar moment of inertia of the circular particles; Ng and Dobry (1992, 1994), fixed the rotational motion completely; and, Iwashita and Oda (1998), included rotational resistance between cylindrical or spherical bodies.

Each of the above mentioned three DEMs, namely i), ii) and iii), have been developed for different types of analyses. Polygon shaped particle based DEMs, for example, Cundall (1971, 1980), and Hocking (1978), have been used to analyze the mechanical behavior of blocky rock masses in mining engineering, and Hocking, Mustoe and Williams (1985,1987), and Hocking (1992,1993) have applied DEMs to arctic engineering problems involving the determination of ice forces on offshore structures and ships. The superquadric DEM (see, Williams and Pentland 1989, Mustoe and DePoorter 1993, Miyata et al. 2000, Mustoe et al. 2000) and ellipsoid DEM (see, Rothenburg and Bathurst 1991, Ting et al. 1993, Ng and Lin 1993, Ng 1994, Sawada and Pradham 1994, Lin et al. 1996, Lin and Ng 1997) are especially useful for problems involving particulate media described by continuous surface geometry. These particle shapes have been mainly used for investigations on the effects of particle shape on static deformation and strength characteristics of particulate media such as sand like materials. The rigid or flexible cluster based DEMs (Walton and Braun 1993, Tsuchikura et al. 1995, Mustoe and Griffiths 1998, Yamane et al. 1998, Itasca Consulting Group 1999) are a simple adaptation of the original circular disk and spherical DEMs developed to assess the effect of non-circular shaped bodies.

2.2 General Theory for Two-dimensional Disc Shaped DEM

A typical DEM has the following features: i) an automatic contact detection algorithm involving a series of sorting actions and geometry checks of increasing complexity, ii) a contact force generation algorithm

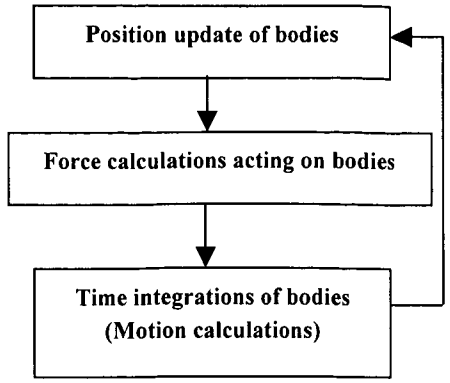

Figure 5 Flow diagram of explicit calculation cycle in DEM

that can either compute total force or incremental force updates, and iii) a time integration procedure which is explicit involving a two step generalized velocity and position update. For further details of the computational algorithm for a typical DEM, see Cundall and Strack (1979a, 1979b) for examples. **Figure 5** shows flow diagram of the explicit calculation cycle in DEM. In this section, basic calculation scheme of circular shaped DEM will be shown briefly.

(1) Basic equations of motion

According to the Newton's second low, the translational equation of motion for the center of mass of body ***i*** within the global system is written as:

$$m_i \ddot{\vec{r}}_i = \sum_k \vec{F}_k + m_i \vec{g} \qquad (1)$$

where m_i is mass of body ***i***, $\vec{r}_i$ is position vector of body ***i***, $\ddot{\vec{r}}_i$ is translational acceleration vector, $\vec{F}_i$ is contact force vector on contact *k*, and $\vec{g}$ is gravitational acceleration vector. **Figure 6** shows a schematic view for this.

Similarly, the rotational equation of motion is written as:

$$I_i \ddot{\theta}_i = \sum_k \vec{M}_k \qquad (2).$$

Note that I_i is moment of inertia of body ***i*** respect to its center of mass, θ is angle of body ***i*** respect to its center of mass, $\ddot{\theta}_i$ is angular acceleration and $\vec{M}_i$ is rotational moment acting body ***i***.

(2) Time stepping scheme for particle motion update

a) Translational motion

Explicit central difference velocity and position update method is employed in particle motion calculations. From the Newton's second low as shown in equation (1), translational acceleration at time step n in the global system can be given by the following equation:

$$\ddot{\vec{r}}_i^{\,n} = \frac{\sum_k \vec{F}_k + m_i \vec{g}}{m_i} \qquad (3).$$

The acceleration and position are defined at time step of n (n=1,2..), while translational velocity is defined at the mid-intervals of ($n\pm1/2$) as shown in **Figure 7**.
The equation of motion, Eq.(3), is integrated using a centered finite-difference procedure by the time step of Δt. This means that a linear acceleration is supposed between two neighboring time steps of acceleration and position. Therefore, new velocity at time step of (n+1/2) can be calculated by using velocity at time step of (n-1/2) and the acceleration at time step n is given as follows:

- Velocity update -

$$\dot{\vec{r}}_i^{\,n+\frac{1}{2}} = \dot{\vec{r}}_i^{\,n-\frac{1}{2}} + \ddot{\vec{r}}_i^{\,n}\Delta t \qquad (4).$$

Then, the new position of body i at time step n is updated by the following equation:

- Position update-

$$\vec{r}_i^{\,n+1} = \vec{r}_i^{\,n} + \dot{\vec{r}}_i^{\,n+\frac{1}{2}}\Delta t \qquad (5).$$

b) Rotational motion

Similar to the above scheme, the new angle of the body i at time step n can be updated by the three following equations.

$$\ddot{\theta}_i = \frac{\sum_k \vec{M}_k}{I_i} \qquad (6)$$

- Angular velocity update -

$$\dot{\theta}_i^{\,n+\frac{1}{2}} = \dot{\theta}_i^{\,n-\frac{1}{2}} + \ddot{\theta}_i^{\,n}\Delta t \qquad (7)$$

- Angle update -

$$\theta_i^{n+1} = \theta_i^{n} + \dot{\theta}_i^{\,n+\frac{1}{2}}\Delta t \qquad (8)$$

From the above integration, new position is updated by the time interval of Δt. Not described here, the time interval has to be small enough to get the stable analyses.

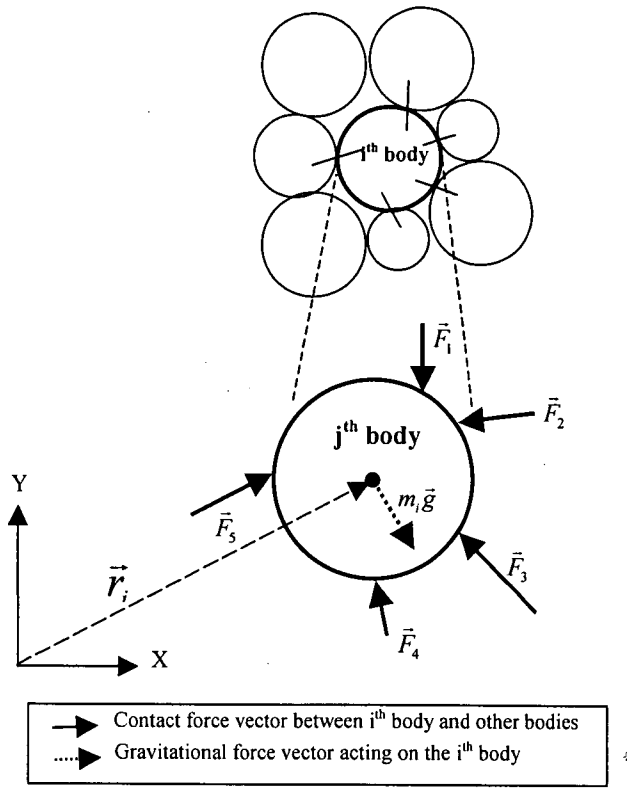

Figure 6 Forces acting on the i^th body

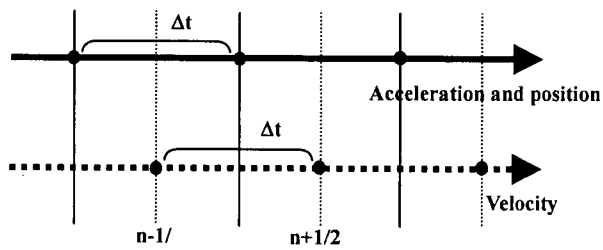

Figure 7 Time stepping scheme

(3) Contact force calculations

In DEM, although the particles are assumed to be rigid for the purpose of particle shape definition, local elastic deformation is allowed to take place at the contacts. In order to calculate contact forces between particles or between particle and wall, the two processes are required; i) contact detection, ii) constitutive model providing a relation between contact force and contact relative displacement in normal and shear direction at contact. Here, the contact detection for circular particles and the representative constitutive models are described.

a) Contact detection and distance of penetration

For the calculation of contact forces between two bodies i and j, firstly, the two bodies are checked

whether they are or not in contact each other. In no-contact conditions, contact forces are not developed between the two bodies. For circular two bodies, a contact can be identified by their center positions and their radii R_i and R_j. **Figure 8** shows a schematic view of a contact between two circular bodies. Here, distance of penetration δ_n is defined as follows:

$$\delta_n = R_i + R_j - \sqrt{(x_i - x_j)^2 + (y_i - y_j)^2} \qquad (9)$$

where R_i and R_j are radii of body i and body j, (x_i, y_i) and (x_j, y_j) are center coordinates in the global system. Therefore, two circular bodies are recognized in contact when the penetration distance, δ_n, has a positive value as shown below.

$$\begin{cases} \delta_n < 0 & (no-contact) \\ \delta_n \geq 0 & (in\ \ contact) \end{cases} \qquad (10)$$

This is the condition of contact between two circular bodies. Between a body and a wall, the same contact detection procedure can be used.

b) Relative velocity and displacements at contacts

Let's suppose that two contacting circular bodies ***i*** and ***j*** have translational velocities $\vec{V}_i$ and $\vec{V}_j$, and angular velocities $\vec{\omega}_i$ and $\vec{\omega}_j$, respectively. **Figure 9** shows a schematic view of the two bodies, whose radii are R_i and R_j respectively, are in contact at point P. Under this condition, velocity at the contact point P of body i ($\vec{V}_{ci}$) and that of body j ($\vec{V}_{cj}$) are given as the following equations:

$$\vec{V}_{ci} = \vec{V}_i + \vec{\omega}_i \times \vec{r}_{ip} \qquad (11a)$$

$$\vec{V}_{cj} = \vec{V}_j + \vec{\omega}_j \times \vec{r}_{jp} \qquad (11b)$$

where $\vec{r}_{ip}$ and $\vec{r}_{jp}$ are branch vectors from each center of the body to the contact point P.

Then, relative velocity at the contact P in the contact normal (V_{rn}) and tangential (V_{rs}) directions with respect to the contact plane can be defined as follows:

$$V_{rn} = (\vec{V}_{cj} - \vec{V}_{ci}) \cdot \hat{n} \qquad (12a)$$

$$V_{rs} = (\vec{V}_{cj} - \vec{V}_{ci}) \cdot \hat{s} \qquad (12b)$$

where $\hat{n}$ is contact normal unit vector and $\hat{s}$ is tangential (shear) direction unit vector at contact point P. As described later, inter-particle forces are calculated by using the penetration distance. The contact point is usually defined at P in the figure. The point P is assigned at middle of the penetration.

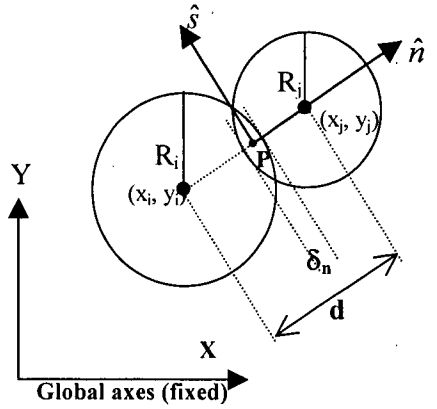

Figure 8 Distance of penetration between two circular bodies

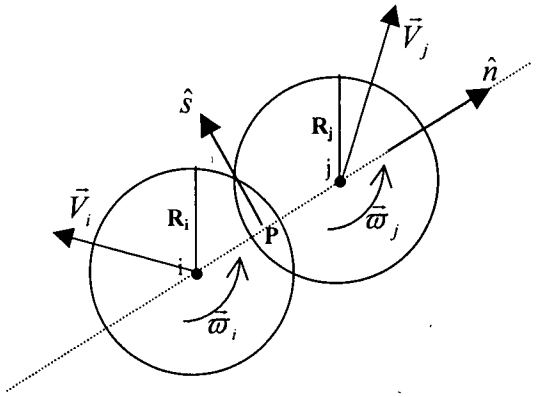

Figure 9 Relative velocities at contact point P

Between particle and wall, the same contact procedure can be used. In this case, relative velocities are obtained by assuming body j is always at rest when the wall is completely fixed. If the wall is moving or rotating, the same procedure is applicable.

c) Contact force model

There are various contact force models (constitutive models), which determine forces generated between two contacting/colliding bodies. The force models provide a relation between contact force and relative displacement in normal and shear direction at contacts. In the procedures of DEM calculations, a contact force model has an important role because inter-particle forces determine the behavior of particle movements. As for elastic contact force, contact force models used for DEM may be categorized into, i) Linear stiffness force model and ii) Hertz-Mindlin theory based force model.

In this section, as a simple force model, the linear stiffness force model with a velocity dependent dashpot in normal direction, and linear stiffness force model

with Coulomb's friction model in shear direction, are introduced. Later, Hertz-Mindlin theory based force model will be shown.

①Linear stiffness model

- Normal direction -

Figure 10 shows a schematic view of this contact model. Contact normal force generated between two contacting bodies is determined by a combination of a normal spring and a velocity dependent damping. The elastic force vector ($\vec{F}_{ne}$) acting on body *i* is determined by the following equation:

$$\vec{F}_{ne} = -k_n \delta_n \hat{n} \tag{13}$$

where k_n is a spring constant.

For the absorbing energy of the system, a velocity dependent dashpot is installed in this force model. The normal damping force vector ($\vec{F}_{nd}$) acting on body *i* is given as follows:

$$\vec{F}_{nd} = c_n \dot{\delta}_n \hat{n} \tag{14}$$

$$\dot{\delta}_n = (\dot{\vec{r}}_j - \dot{\vec{r}}_i)\hat{n} \tag{15}$$

where c_n is a damping coefficient. Therefore, the total force vector in contact normal direction is calculated by adding the elastic force and the damping force as shown below:

$$\vec{F}_n = \vec{F}_{ne} + \vec{F}_{nd} \tag{16}.$$

In this model, damping coefficient c_n can be calculated by using mass of two contacting bodies (m_1 and m_2), the coefficient of restitution e and the normal spring constant k_n based on the following equation. The equation is obtained by an analytical method as,

$$c_n = 2 \cdot \ln\left(\frac{1}{e}\right) \cdot \sqrt{\frac{k_n \cdot m^*}{\pi^2 + \left[\ln\left(\frac{1}{e}\right)\right]^2}} \tag{17}$$

where m^* is the effective mass as shown below:

$$m^* = \frac{m_1 m_2}{m_1 + m_2} \tag{18}.$$

- Tangential direction -

The tangential (shear) force is determined by a combination of an elastic shear spring and a frictional slider in this contact model as shown in **Figure 11**. The tangential contact force is computed in an incremental fashion. When the contact is formed, the shear force is initialized at zero. The incremental shear force within time step Δt is calculated by the following equation.

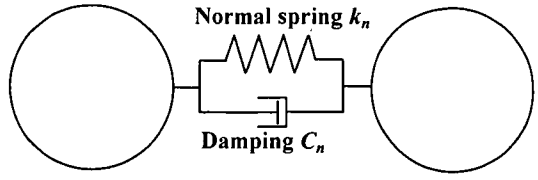

Figure 10 Linear stiffness contact model with a velocity dependent dashpot in normal direction

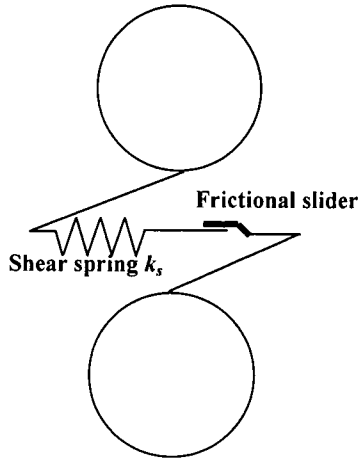

Figure 11 Linear stiffness contact model with a friction slider in tangential direction

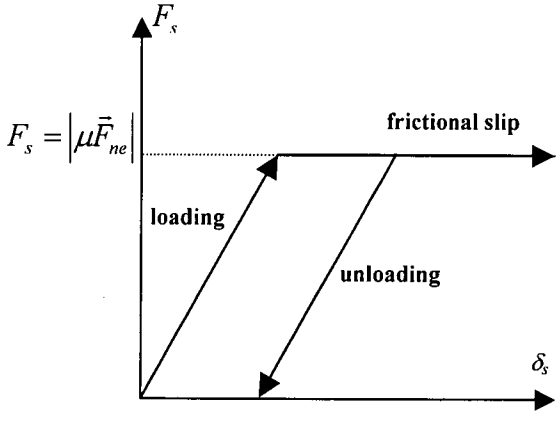

Figure 12 Constitutive behavior in the tangential direction at contact points

$$\Delta F_s = k_s \Delta \delta_s \tag{19}$$

where $\Delta \delta_s$ is an incremental shear displacement due to the relative tangential velocity at contact. This δ_n is expressed as below:

$$\Delta \delta_s = (\dot{\vec{r}}_j - \dot{\vec{r}}_i)\hat{s}\Delta t \tag{20}.$$

The new shear force is then calculated by adding each incremental shear force to the current shear force as shown below:

$$F_s = F_s + \Delta F_s \quad (21).$$

If the updated shear force exceeds its limit value defined by the Coulomb limit, the new shear force is given as its maximum value. The maximum value is simply defined by the multiplying friction coefficient μ by the elastic normal force as shown below:

$$F_s = sign(\Delta\delta_s)\left|\mu\vec{F}_{ne}\right| \quad \text{if} \quad \left|F_s\right| \geq \left|\mu\vec{F}_{ne}\right| \quad (22).$$

Therefore, the shear force vs. relative shear-displacement relationship is plotted as **Figure 12**. Finally, the shear force vector can be calculated by the following equation:

$$\vec{F}_s = F_s\hat{s} \quad (23).$$

②Hertz-Mindlin based contact models for DEM

In accrual contacts between two elastic bodies, the contact force-displacement relation depends on the material properties of the particles and the surface conditions. Force-displacement relations in both normal and tangential directions for two elastic spheres with friction can be provided by theories of Hertz (see Johnson, 1985), Mindlin(1949) and Mindlin & Deresiewicz(1953). For further information about the contact force theories, see the references shown above.

The most sophisticated contact model for DEM is the use of the above contact theory. We call such contact force models as "Hertz-Mindlin contact model". According to Dobry and Ng (1989), Hertz-Mindlin contact force models for DEM can be categorized into the following three models in the order of the complexity of modeling. For further information about the first model, see for example Seridi and Dobry (1984), about the second, see for example Thornton and Randall (1988).

- Complete Hertz-Mindlin model
- Simplified Hertz-Mindlin model
- Linear pressure dependent model

In the next session, we describe the linear pressure dependent model for DEM (the third model) since we choose this model for the three-dimensional ellipsoidal DEM. Here we also describe the Hertz-Mindlin contact theory.

- Normal direction -

The Hertz theory deals with a pair of homogenous, isotropic, elastic solids in contact due to forces that are normal to their initial common tangent plane. From the theory, we obtain a relationship between the normal contact force N and the relative normal approach displacement α_n. The relationship between two contacting spheres "*1*" and "*2*", whose radii are R_1 and R_2, is given as,

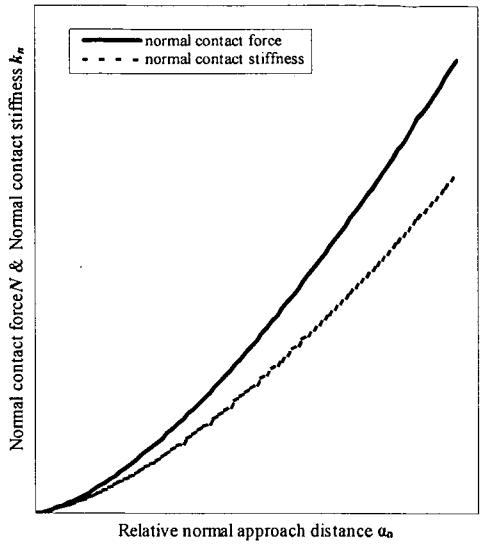

Figure 13 Constitutive behavior of two identical elastic spheres by Hertz-contact theory

$$N = \frac{4}{3}E^*\left(R^*\alpha_n^{\,3}\right)^{1/2} \quad (24)$$

where E^* and R^* are constants which are determined by material properties such as radius, Young's modulus and Poisson's ratio of each sphere. E^* and R^* are defined as,

$$\frac{1}{E^*} = \frac{(1-\upsilon_1)^2}{E_1} + \frac{(1-\upsilon_2)^2}{E_2} \quad (25)$$

and

$$R^* = \frac{2R_1R_2}{R_1+R_2} \quad (26)$$

where υ and E are Poisson's ratio and Young's modulus of each sphere. **Figure 13** shows a schematic relationship between the normal force and the relative normal displacement. Note that the relation is not linear between two elastic spheres.

The derivative of the equation (24) gives the normal stiffness k_n at contacts as follows:

$$k_n(\alpha_n) = \frac{\partial N}{\partial \alpha_n} = 2E^*\left(R^*\alpha_n\right)^{1/2} \quad (27).$$

We find that the normal stiffness is dependent on the normal approach displacement. See **Figure 13**, we find that the stiffness becomes greater as increasing of the

normal approach displacement. Note that this relation is also dependent on the material properties of the two contacting particles. If we use a linear stiffness model (k_n=constant) for the normal contact calculation, we cannot consider the effects of the particle stiffness. Therefore, this normal contact model is required especially for the situation where particles are compressed at high pressures. Note that the normal stiffness has to be calculated according to the two materials' properties in contact and the current overlap distance between the particles, which is resulting in consuming much computational CPU time than the liner stiffness model. Therefore, we choose this contact model for the

- Tangential direction -

Closed form solutions for tangential contact stiffness between two identical elastic spheres for a variety of instantaneous rates of normal and tangential forces are found in Mindlin & Deresiewicz (1953). In this theory, the shear force parallel to the initial common tangent plane of the contacting two solids is added to the original Hertz theory. However, the tangent contact law is more complicated than the Hertz theory in the following points.

- There is a permanent tangential displacement due to tangential loading and it results in non-linear relations between the shear force and the displacement with energy dissipation.
- The tangential stiffness is dependent on the normal force. Therefore, a combination of the normal and the tangential forces must be taken into account.
- The tangential stiffness is dependent on the full loading history of both normal and tangential forces and also on the current forces.

As mentioned before, there may be three levels of Hertz-Mindlin contact model used for DEMs. The linear pressure dependent model for the tangential direction contact, which is the simplest model among them, is described here.

The model is also based on the work by Mindlin (1949) and it showed that the relation between relative tangential displacement α_s and tangential force S between two spheres with friction coefficient μ for a constant normal force N under a monotonic increasing loading condition. The relation is expressed as follows:

$$\alpha_s = \left(\frac{3\mu N}{16G^* a}\right)\left[1-\left(1-\frac{S}{\mu N}\right)^{2/3}\right] \qquad (28)$$

where a is the radius of the contact area between two contacting spheres;

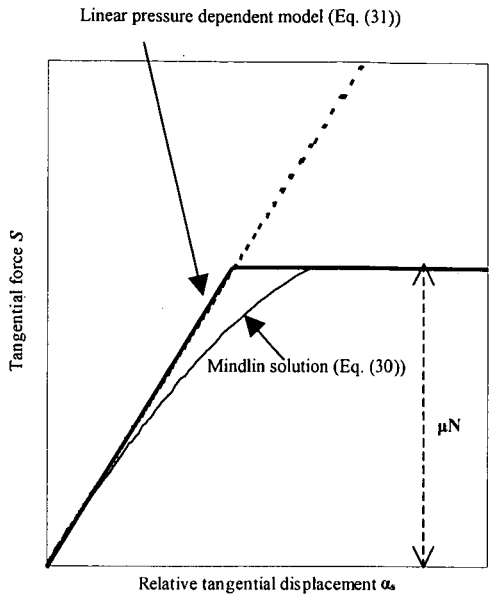

Figure 14 Tangential constitutive behavior of two identical elastic spheres

$$a = \left(\frac{3NR^*}{4E^*}\right)^{1/3} \qquad (29a)$$

and G^* is,

$$\frac{1}{G^*} = \frac{(2-\upsilon_1)}{G_1} + \frac{(2-\upsilon_2)}{G_2} \qquad (29b)$$

where $G_{1,2}$ is shear modulus. Therefore, the tangential stiffness at contact is given by the derivative of the equation (28) as follows:

$$k_s(N,S) = \frac{1}{\dfrac{\partial \alpha_s}{\partial S}} = \frac{\partial S}{\partial \alpha_s} = 8G^* a\left(1-\frac{S}{\mu N}\right)^{1/3} \qquad (30).$$

As shown in the above equation, the tangential stiffness is dependent on the current contact forces N and S. As this tangential stiffness model still requires much computer time, in the third model the stiffness at $S=0$ is employed at any tangential force for simplicity. Therefore, the tangential stiffness is expressed simply as below:

$$k_s(N,S=0) = 8G^* a = 8G^*\left(\frac{3R^*}{4E^*}\right)^{1/3}(N)^{1/3} \qquad (31).$$

This tangential stiffness model is called as the "Linear pressure dependent contact model" and the stiffness is dependent only on the current normal contact force. The tangential stiffness given by equations (30) and (31) are plotted against the relative tangential displacement α_s in **Figure 14**.

(4) Mechanical damping models

In the linear stiffness contact model, the kinetic energy of the system is absorbed only by the normal dashpot and the shear friction. In addition to these dumping factors, there are several additional damping models, which effectively absorb the kinetic energy of the system. Here, two representative models, which absorb kinetic energy in time stepping scheme, are described.

a) Velocity and mass dependent damping

This damping system assumes that a moving body always has force that is acting opposite to the body's velocity direction. The damping force is dependent on both mass and velocity of the body. A damping term is added to the original equation of motions as follows:

$$m_i \ddot{\vec{r}}_i = \sum_k \vec{F}_k + m_i \vec{g} - \alpha_t m_i \dot{\vec{r}}_i \qquad (32a)$$

$$I_i \ddot{\theta}_i = \sum_k \vec{M}_k - \alpha_r I_i \dot{\theta}_i \qquad (32b)$$

where α_t is a proportionality constant for the global translational dumping coefficient and α_r is the same constant for the global rotational damping coefficient. With this damping model, the kinetic energy of the system is absorbed at every time step of the motion integration.

b) Local non-viscous damping

Local non-viscous damping is similar to that described in Cundall (1987) and is used in a commercial codes PFC2D and PFC3D (Itasca Consulting Group, Inc., 1999). A damping term is added to the original motion of equations as follows:

$$m_i \ddot{\vec{r}}_i = \sum_k \vec{F}_k + m_i \vec{g} - \alpha_t' \left| \sum_k \vec{F}_k \right| sign(\dot{\vec{r}}_i) \qquad (33a)$$

$$I_i \ddot{\theta}_i = \sum_k \vec{M}_k - \alpha_r' I_i \left| \sum_k \vec{M}_k \right| sign(\dot{\theta}_i) \qquad (33b)$$

where α'_t is a damping constant for the global translational motion and α'_r is for the global rotational motion.

2.3 The Two-Dimensional Superquadric DEM

The most general of DEMs, are the polygon based and cluster based DEMs since they can model arbitrary shaped non-symmetrical particles/bodies. However, if we want to investigate the effects of particle shape in a parametric manner, it is advantageous for us to use DEMs employing an analytical representation for the particle shape. Here, we introduce a superquadic representation of two-dimensional particle shape. In this section, 2.3, we only describe the characteristics of the particle shape modeled by superquadric functions, the contact detection algorithms and the contact force determination for the two-dimensional superquadric particles since the other calculation procedures remain same as the above mentioned circular or sphere shaped DEMs in 2.2.

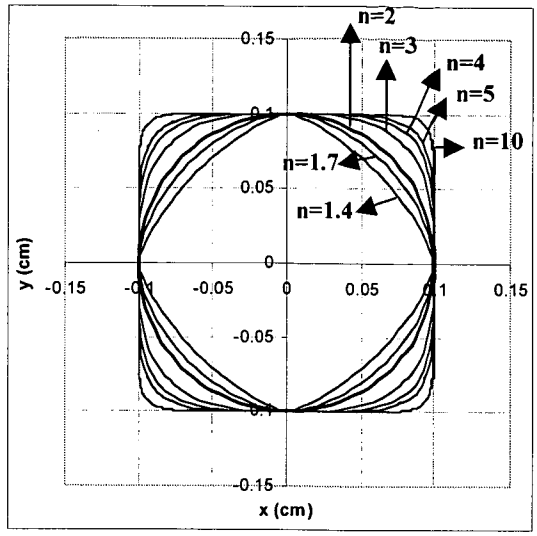

Figure 15 Shapes of the superquadric shaped particles
(n: the exponent coefficient in equation (34))

(1) The superquadric function

In the superquadric DEM, the boundary geometry for a body "i" is defined with respect to the local centroidal coordinates as follows:

$$f_i(x_i, y_i) \equiv \left(\frac{|x_i|}{a_i} \right)^{n_i} + \left(\frac{|y_i|}{b_i} \right)^{n_i} - 1 \qquad (34)$$

where the point $P(x_i, y_i)$ is: i) outside the body when $f_i(x_i, y_i) > 0$, ii) inside the body when $f_i(x_i, y_i) < 0$ and iii) on the surface when $f_i(x_i, y_i) = 0$. Note, a_i and b_i are the semi axes of the superquadric that define the aspect ratio of the bounding rectangle, and the exponent n_i is a real number that determines the shape of the superquadric in terms of angularity. The term angularity should be regarded as a measure of the maximum curvature on the surface of a superquadric. Examples of different superquadric shapes with the shape exponents n = 1.4, 1.7, 2.0, 3.0, 5.0 and 10.0 are illustrated in **Figure 15** for a fixed aspect ratio of 1.0. Note, from this figure, we can conclude that superquadrics have sharp corners with discontinuous tangent planes for two limiting values of n. For n = 1, the superquadric is a parallelogram with corners on the local centroidal x and y axes, and as $n \to \infty$, the superquadric becomes a rectangle with sides of length $2a$ and $2b$, that are parallel to the local centroidal x and y axes. In this work,

we have limited our consideration to the superquadric shaped bodies with smooth convex surface geometry, where the shape exponent n is usually defined in the range $1 < n \leq 10$. This choice of n allows a wide range of non-circular shaped bodies to be modeled, and avoids the inherent mathematical difficulties encountered when $n > 10$ or $n < 1$.

Figure 16 shows two superquadric shaped bodies "*i*" and "*j*" defined by $f_i(x_i, y_i) = 0$ and $f_j(x_j, y_j) = 0$ respectively. When the point $P(x_i, y_i)$ is on the surface of the body "*i*", the local coordinates can be defined with the two parametric equations:

$$x_i(\alpha_i) = a_i\, sign(\cos(\alpha_i))\left|\cos(\alpha_i)\right|^{2/n_i}, \qquad y_i(\alpha_i) = b_i\, sign(\sin(\alpha_i))\left|\sin(\alpha_i)\right|^{2/n_i} \tag{35}$$

where α_i is a parametric angle.

(2) Contact detection between superquadric bodies

In the superquadric based DEM algorithm, contact between two bodies "*i*" and "*j*" is determined by computing the minimum overlap distance with a minimization procedure, which is based on a geometric potential concept, in the following manner:

a) Find the point P_i that is on the surface of the body "*i*" and minimize the superquadric function for body "*j*" as shown in **Figure 17**. Since the point P_i is on the surface of the body "*i*", the coordinates of P_i with respect to the local centroidal axes of body "*i*" are defined by the parametric equations (35) which depend on the parameter α_i. In order to minimize $f_j(x_j, y_j)$ which is defined by:

$$f_j(x_j, y_j) \equiv \left(\frac{|x_j|}{a_j}\right)^{n_j} + \left(\frac{|y_j|}{b_j}\right)^{n_j} - 1 \tag{36}$$

the coordinates of the point P_i must be expressed with respect to the local centroidal axes of body "*j*". This is accomplished with the coordinate transformation:

$$\begin{bmatrix} x_j(\alpha_i) \\ y_j(\alpha_i) \end{bmatrix} = \begin{bmatrix} \cos(\theta_j - \theta_i) & -\sin(\theta_j - \theta_i) \\ \sin(\theta_j - \theta_i) & \cos(\theta_j - \theta_i) \end{bmatrix} \begin{bmatrix} x_i(\alpha_i) \\ y_i(\alpha_i) \end{bmatrix} + \begin{bmatrix} x_o \\ y_o \end{bmatrix} \tag{37}$$

where (x_o, y_o) are the coordinates of the centroid of body "*j*" with respect to body "*i*" defined in the local centroidal coordinate axes of body "*i*", and θ_i and θ_j are the angular coordinates defining the local x-directions for body "*i*" and body "*j*" with respect to the global x-direction respectively.

The location of the point P_i is now determined by minimizing the function $f_j(x_j(\alpha_i), y_j(\alpha_i)) = 0$ with respect to the parameter α_i. The point P_j that is on the surface of the body "*j*" which minimizes the superquadric function for body "*i*" is determined in exactly the same manner.

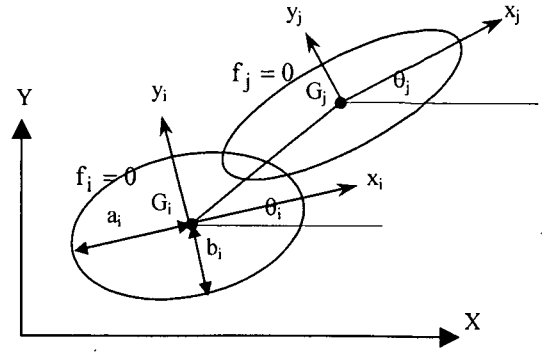

Figure 16 Two Superquadric Shaped Bodies "i" and "j" in Contact

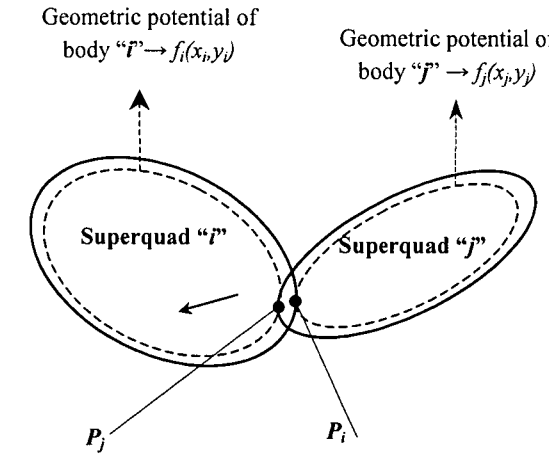

Figure 17 Contact detection of superquadric particles based on geometric potential

b) Determine the radii and centers of curvature at the two contact points P_i and P_j. Firstly, note that the radius of curvature ρ_k at the point P_k is given by the standard formula below for a curve defined by $y = f(x)$:

$$\rho_k = \left(1 + \left(\frac{dy_k}{dx_k}\right)^2\right)^{3/2} \Bigg/ \frac{d^2 y_k}{dx_k^{\,2}}, \quad k = i, j \tag{38}$$

For a superquadric curve defined by $f_k(x_k, y_k) = 0$,

equation (38) becomes:

$$\rho_k = \frac{\left(\left(\frac{\partial f_k}{\partial x_k}\right)^2 + \left(\frac{\partial f_k}{\partial y_k}\right)^2\right)^{3/2}}{\left(\frac{\partial^2 f_k}{\partial {x_k}^2}\left(\frac{\partial f_k}{\partial y_k}\right)^2 - 2\frac{\partial^2 f_k}{\partial y_k \partial x_k}\frac{\partial f_k}{\partial x_k}\frac{\partial f_k}{\partial y_k} + \frac{\partial^2 f_k}{\partial {y_k}^2}\left(\frac{\partial f_k}{\partial x_k}\right)^2\right)} \qquad k = i, j \tag{39}$$

The unit outward normal vector on the surface of body "k" defined by a superquadric in the local centroidal coordinate system for body "k" is given by:

$$\hat{n}_k = \nabla f_k / |\nabla f_k| = \begin{bmatrix} n_x \\ n_y \end{bmatrix}_k \qquad k = i, j \tag{40}$$

The coordinates with respect to the centroidal local axes of body "k" for the position of the center of curvature C_k, for the point P_k is given by:

$$\begin{bmatrix} c_x \\ c_y \end{bmatrix}_k = \begin{bmatrix} x_k \\ y_x \end{bmatrix} - \rho_k \begin{bmatrix} n_x \\ n_y \end{bmatrix}_k \qquad k = i, j \tag{41}$$

c) Compute the normal penetration distance between the two contacting bodies "i" and "j". If the contact problem is reduced to contact between the two circles of curvature shown in **Figure 18**, the normal overlap or the penetration distance is defined by:

$$\delta_n = \rho_i + \rho_j - d \tag{42}$$

where d is the distance between the center of curvatures C_i and C_j. Note that the contact between bodies "i" and "j" exists when $\delta > 0$.

The contact normal direction for bodies "i" and "j" is defined by a unit vector $\hat{n}_{ij}$ directed along the center of curvatures from C_i to C_j as shown in **Figure 18**. The corresponding contact shear direction is defined by a unit vector $\hat{s}_{ij}$ that is obtained with a counterclockwise rotation of 90° of $\hat{n}_{ij}$.

In the current DEM calculation, we have employed the usual linear stiffness contact model with restitution and the Coulomb friction model. In the present algorithm, the Brent method (Brent 1971) is used to perform the superquadric function minimizations. The incremental iterative updates for calculation parameters are used to improve the efficiency of the computation as well. Look up tables are also used to decrease the effort for the computation of power functions required in the superquadric equations.

- P_i and P_j are the two boundary points that minimize the superquadric geometric potentials.
- C_i and C_j are the center of curvatures at P_i and P_j respectively.

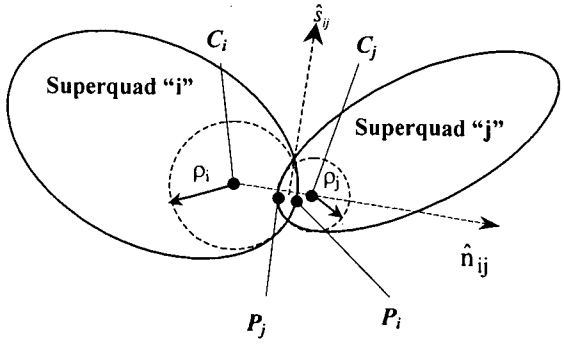

Figure 18 Contact parameters for two contacting superquadric shaped bodies

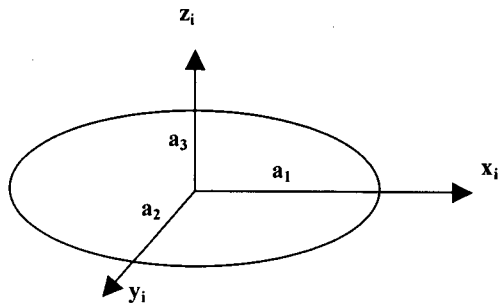

Figure 19 Definition of ellipsoidal particle

2.4 The Three-Dimensional Ellipsoid DEM

The three-dimensional ellipsoidal discrete element model employed in this work, originated from the DEM algorithm developed by Lin for studying soil behavior, see Lin (1995), Lin, Nakagawa and Mustoe (1996), and Lin and Ng (1995, 1997). The details of the dynamic time stepping scheme and the ellipsoidal particle-particle contact detection and force generation algorithm are fully described in Lin (1995). In this section, we briefly describe the contact detection and contact laws of ellipsoidal particles. In addition to them, we also describe the details of the contact detection between an ellipsoidal particle and a triangular face (Mustoe and Miyata, 2001).

(1) Contact detection between ellipsoidal particles

The three-dimensional ellipsoidal particle shapes are defined by the semi-axis values a_1, a_2 and a_3 as shown

in **Figure 19**. Using local coordinate system, the equation of the ellipsoid's surface is expressed as follows:

$$f(x_1,x_2,x_3)=\left(\frac{x_1}{a_1}\right)^2+\left(\frac{x_2}{a_2}\right)^2+\left(\frac{x_3}{a_3}\right)^2-1=0 \quad (43).$$

A wide range of different shaped particles can be modeled with different values of a_1, a_2 and a_3. With the equation (43), tablet, football and spherical shapes are generated with (a_1:a_2:a_3) ratios of (2:2:1), (2:1:1) and (1:1:1) respectively.

Similar to the 2D model in the previous section, we apply a contact detection algorithm based on the geometric potential concept for the Ellipse 3D. A brief description is given here (for more details, see Lin & Ng (1995,1997). For the ellipsoidal particle, a geometric potential is given as follows:

$$f(x_1,x_2,x_3)=\left(\frac{x_1}{a_1}\right)^2+\left(\frac{x_2}{a_2}\right)^2+\left(\frac{x_3}{a_3}\right)^2-1 \quad (44).$$

By using geometric potentials, the points P_i and P_j are obtained as shown in **Figure 20**. In the figure, solid line is surface of ellipsoid and dotted line is geometric potential.

The normal and tangential contact force laws between ellipsoidal particles are slightly different from those between spheres since the particle shape is different. As illustrated in **Figure 21**, a small elliptic contact interface in the contact tangent plane is generally formed when two curve solid surfaces (solid and dotted lines) are in contact. This elliptic contact interface can be expressed by axes, u and v, as follows:

$$Au^2+Bv^2=h \quad (45)$$

where h is the initial separating distance of the two curved surfaces on the elliptic interface. The positive constants A and B are given from the following relations:

$$A+\mathrm{B}=\frac{1}{2}\left(\frac{1}{R_1'}+\frac{1}{R_1''}+\frac{1}{R_2'}+\frac{1}{R_2''}\right) \quad (46a)$$

$$\mathrm{B-A}=\frac{1}{2}\left[\left(\frac{1}{R_1'}-\frac{1}{R_2'}\right)^2+\left(\frac{1}{R_1''}-\frac{1}{R_2''}\right)^2+2\left(\frac{1}{R_1'}-\frac{1}{R_2'}\right)\left(\frac{1}{R_1''}-\frac{1}{R_2''}\right)\cos(2\beta)\right]^{1/2} \quad (46b)$$

in which R_1', R_1'', and R_1', R_2'' are the principal radii of curvature of the two solid surfaces at contact point, and β is the angle between major principle directions of curvature of the two surfaces as shown in **Figure 21**. The angle η between axes u_1 and u_2 can be

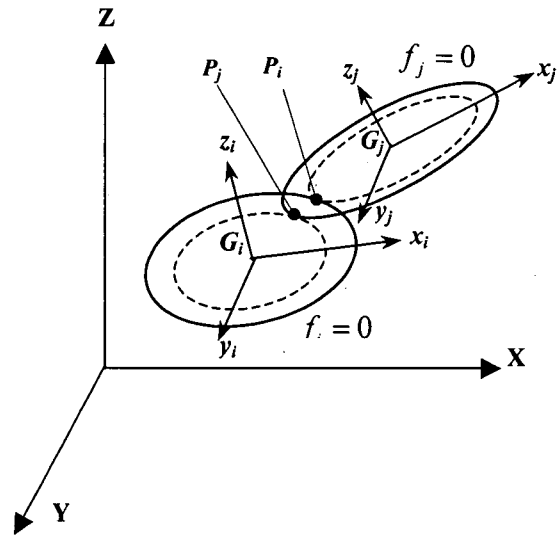

Figure 20 Two ellipsoidal shaped bodies "i" and "j" in contact

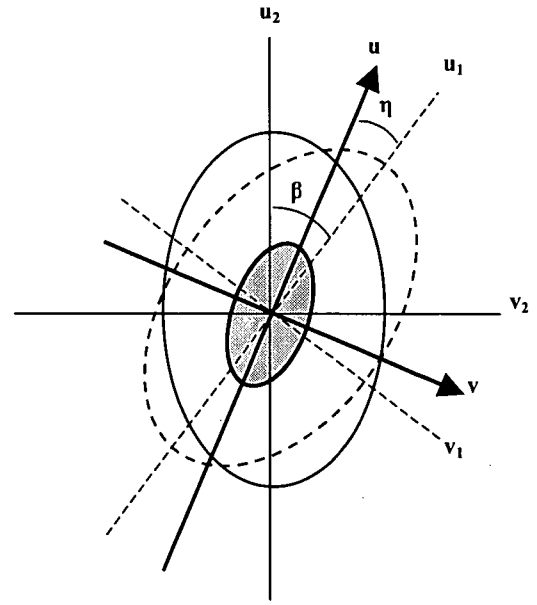

Figure 21 Two ellipsoidal shaped bodies "i" and "j" in contact

specified with R_1', R_1'', R_1', R_2'' and β (Boresi and Sidebottom, 1984).

As a general form, the Hertzian normal contact law is given as follows:

$$N=\frac{4}{3}E^*\left(R_e\alpha_n{}^3\right)^{1/2}\psi(B/A) \quad (47)$$

where $\psi(B/A)$ is an elliptic integral varying with B/A, and R_e is an equivalent radius of curvature, which can be expressed as:

$$R_e = \frac{1}{\sqrt{AB}} \qquad (48).$$

The elliptic integral $\psi(B/A)$ is unity for the contact between spheres and is decreasing slowly from unity with increase of $(B/A)^{1/2}$ (see, Johnson 1985). Therefore, in the current model, $\psi(B/A)$ is given as unity regardless of the principal radii of curvature of the two ellipsoids at contact.

The major and minor principal radii of curvature at any given point of an ellipsoidal surface, R' and R'', can be given by Lipschutz (1969).

Tangential contact force law for general curved solid surfaces in contact is given by Mindlin (1949). The tangential stiffness generally varies with the direction in the contact tangent plane. However, the variation is small. Therefore, for simplicity of the calculation, we use a linear dependent stiffness model shown in the equation (31) in all directions as follows:

$$k_s = 8G^* a = 8G^* \left(\frac{3R_e}{4E^*}\right)^{1/3} (N)^{1/3} \qquad (49).$$

(2) Contact detection between ellipsoidal particle and triangular face

The details of the contact detection between an ellipsoidal particle and a triangular face are described here. For the simplification of the development, the equation of the ellipsoid's surface and the equation of the plane for the triangular face with nodes I, J and K are expressed with respect to the principal axes (x_1, x_2, x_3) of the ellipsoidal particle as shown in **Figure 22**. The equation of the plane for the triangular face is given as follows:

$$n_1 x_1 + n_2 x_2 + n_3 x_3 - d_0 = 0, \qquad (50)$$

where d_0 is the distance from the plane to the center of the ellipsoid.

The two possible locations of the nearest point to the plane on the ellipsoid are at P_1 and P_2, where the outward normal direction of the ellipsoid and the unit normal vector, $\hat{n}_f$, of the plane are parallel. This condition is expressed by:

$$\frac{\partial f}{\partial x_i} = \lambda n_i, \qquad i = 1,2,3 \qquad (51)$$

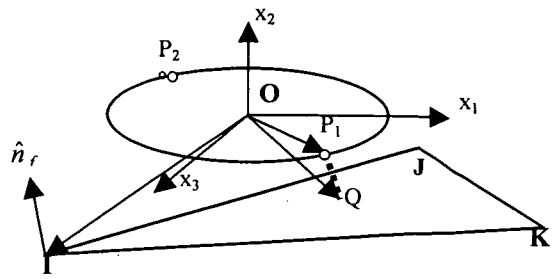

Figure 22 Geometry of an ellipsoidal particle and a triangular face IJK

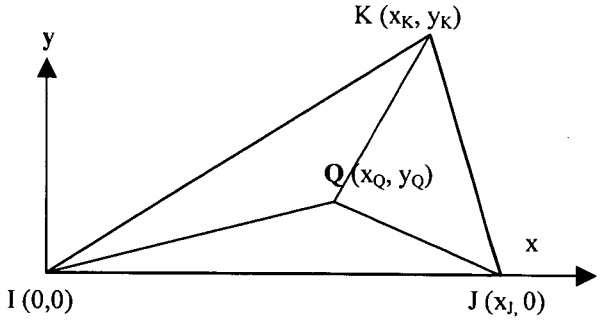

Figure 23 Definition of the two-dimensional local face coordinate system

where $\hat{n}_f = (n_1, n_2, n_3)$ is the unit normal vector of the plane written with respect to the principal axes of the ellipsoid,

$$\lambda = \pm\left[\left(\frac{\partial f}{\partial x_1}\right)^2 + \left(\frac{\partial f}{\partial x_2}\right)^2 + \left(\frac{\partial f}{\partial x_3}\right)^2\right]^{1/2}, \qquad (52)$$

and $$\frac{\partial f}{\partial x_i} = \frac{2x_i}{{a_i}^2}, \qquad i = 1,2,3 \qquad (53).$$

Combining equations (51), (52) and (53), the coordinates $({x_1}^P, {x_2}^P, {x_3}^P)$ of the points P_1 and P_2 are given by:

$${x_i}^P = \frac{\lambda {a_i}^2 n_i}{2}, \qquad i = 1,2,3 \qquad (54).$$

The normal distance δ_n, from the point P_1 (or P_2) to the plane is computed via:

$$\delta_n = n_1({x_1}^I - {x_1}^P) + n_2({x_2}^I - {x_2}^P) + n_3({x_3}^I - {x_3}^P), \qquad (55)$$

where $({x_1}^P, {x_2}^P, {x_3}^P)$ and $({x_1}^I, {x_2}^I, {x_3}^I)$ are the coordinates of the point P_1 (or P_2) and the point I respectively. The point P which closest to the plane is

either located at the point P_1 or P_2 and is determined from the minimum value of the two possible values of δ_n.

The coordinates (x_1^q, x_2^q, x_3^q) of the normal projected point Q from the closest point P on the ellipsoid are given by:

$$x_i^q = x_i^p + \delta_n n_i, \qquad i = 1,2,3 \qquad (56).$$

In order to determine whether the point Q on the plane is inside or outside the triangular face, we compute the triangular coordinates (L_I, L_J, L_K) of the point Q in the following manner. In **Figure 23**, we view the triangular face from the normal unit direction, $\hat{n}_f$, and define the local two-dimensional face coordinate system (x, y) as shown.

From **Figure 23**, we can also define the area of the triangular face *IJK*, by A, and the sub-areas A_I, A_J and A_K as the areas of the triangles *JKQ*, *KIQ* and *IJQ* respectively. These areas are computed by:

$$A = 0.5(x_{JI} y_{KI} - y_{JI} x_{KI}), \qquad (57)$$

$$\begin{aligned} A_I &= 0.5(x_{JQ} y_{KQ} - y_{JQ} x_{KQ}) \\ A_J &= 0.5(x_{KQ} y_{IQ} - y_{KQ} x_{IQ}) \\ A_K &= 0.5(x_{IQ} y_{JQ} - y_{IQ} x_{JQ}) \end{aligned} \qquad (58)$$

where $x_{IJ} = x_I - x_J$, etc..., and $x_I = y_I = y_J = 0$.

The triangular coordinates (L_I, L_J, L_K) of the point Q are then defined by:

$$(L_I, L_J, L_K) = \left(\frac{A_I}{A}, \frac{A_J}{A}, \frac{A_K}{A}\right) \qquad (59).$$

The conditions for the contact between the ellipsoidal particle and the triangular plane IJK are that $\delta_n > 0$ and all three triangular coordinates $(L_I, L_J, L_K) > 0$, otherwise there is no contact. Also, because the triangular coordinates have the normalized property: $L_I + L_J + L_K = 1$, a small positive value of a triangular coordinate indicates that the ellipsoid is close to an edge or corner of the triangular face.

The normal and shear components of the contact force can be then computed in the usual manner employed in a standard DEM for either linear or non-linear force laws.

3. DEM Analyses on Force Support Systems of Particulate Media

3.1 Introduction

As mentioned before, more basic studies on force support systems of particulate media are required for a better understanding on the support systems of rubble rock foundations. In order to investigate the mechanical behavior of the rubble rocks near the surface of the foundation subject to vertical loading, we should simulate the movement of the rubble rocks accurately. Discrete Element Method (DEM) simulations are best suited for this type of complex investigation since we are able to trace the movement of each rubble rock and estimate the magnitude of contact forces between the rocks, and between the rocks and the bottom slab of a caisson during loading.

In order to model the vertical loading history of the foundation due to the weight of a caisson, a series of uniaxial compression test simulations are conducted on a system of both two-dimensional superquadric particles and three-dimensional ellipsoidal particles. In this chapter, the above two simulation results will be presented.

3.2 Uniaxial Compression Test Simulations using two-dimensional superquadric DEM

Circular particles are usually used in DEM simulations, however, actual rubble rocks have very irregular shapes, which affects the local rearrangement of rubble rocks near the surface. In this study, we employ a superquadrics representation of particle shape in order to access particle shape effects in a simple way.

With using the two-dimensional superquadric DEM, we investigate the effects of surface roughness and particle shape on force system of the foundation subject to vertical loading by a caisson. A series of uniaxial compression test simulations are conducted on a system of circular particles and a system of almost rectangular particles. Based on the simulation results, some preliminary observations and discussions on the effects of the surface roughness and the particle shape on the overall mechanical behavior of the foundation will be given here.

(1) Simulation method

Figure 24 shows a procedure for simulating the uniaxial compression test. In the simulation, mono-size particles are inserted in a rectangular box where both sides are periodic boundaries to minimize the boundary effects (**Figure 24 (a)**). After the settlement of particles by the gravity force within the box, the roughness of the sample surface is varied. In the actual construction

Table 1 Simulation cases

CASE	particle shape		surface	sample zize
	shape	semi-axis lengths		
CS	circular (n=2)	a = 15cm	smooth	2.7m (height)
CR		b = 15cm	rough	
SS	superquadric (n=4)	a=19.5cm,	smooth	10m (width)
SR		b=9.76cm	rough	

where a smooth surface roughness of ±5cm is required, relatively large rocks are placed near the foundation surface so that their flat surface face toward the bottom slab of a caisson. In addition to rearranging the large rocks, relatively small rocks are also used to fill in the gaps between the large rocks so that the large rocks cannot move or rotate. Because it was impossible for us to reproduce the actual construction procedures to control roughness in the current simulation, two different types of surface roughness are defined. As shown in **Figure 24 (b)**, one is defined as a "smooth" surface and the other is defined as a "rough" surface. For the smooth surface, particles whose centers are located higher than a certain height are removed. Though some minor irregular roughness of the surface still remains, we call this a smooth surface. For the rough surface, particles whose centers are located higher than a given sinusoidal function are removed. This surface is considered to have large-scale roughness. After varying surface roughness, each sample is allowed to settle again to reach its static equilibrium (**Figure 24(c)**).

After settlement, a loading plate is placed at the maximum height of the sample as shown in **Figure 24(d)**. The plate remains horizontal and is lowered at a constant velocity in the vertical direction. The velocity is small enough for the system to maintain quasi-static behavior of the particles. During calculations, the total vertical load acting on the plate and settlement of the plate are recorded. Contact conditions such as the number, locations, force amplitude of contact points between the loading plate and particles beneath the plate are also recorded. Movements and rotations of all the particles and contact force between particles are also recorded.

(2) Calculation conditions

In the present study, four different samples are used as shown in **Table 1**. In order to identify the effects of non-circular particle shape, we use circular and almost

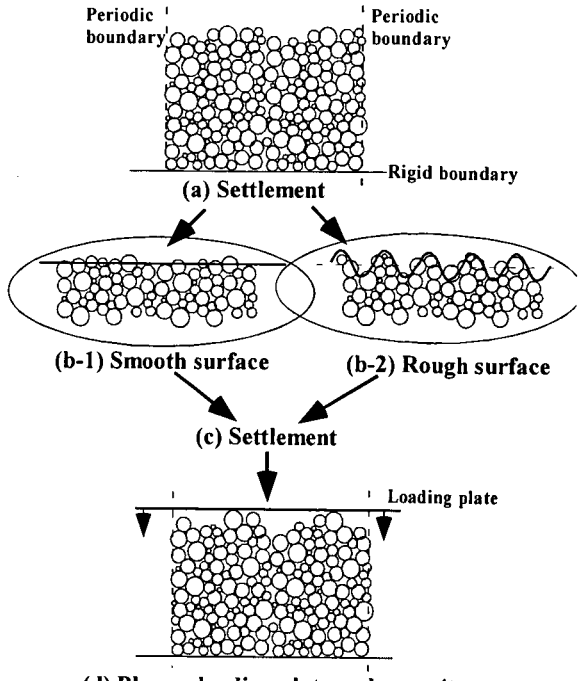

Figure 24 A procedure for uniaxial compression simulation

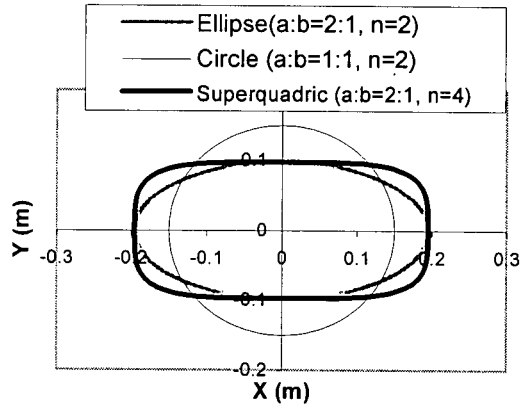

Figure 25 Supequadric representation of particle shape

rectangular particles as shown in **Figure 25**. For the circular particle, a radius of 0.15m is given. We employ a ratio of 2 between major to minor axes for the rectangular particles with the exponent n=4. The size of the rectangular particle is set so that its mass is equivalent to that of the circular particle.

Two different types of surface roughness are studied as mentioned in the previous section. The sample height is set at about 2.7m from the bottom plate in all the cases. For the smooth surface cases, particles whose centers are located higher than 2.7m, are removed. For

the rough surface cases, particles whose centers are located higher than the following sinusoidal function:

$$z(x) = z_0 + a \times \sin\left(\frac{2\pi x}{L}\right) \qquad (60)$$

are removed. In equation (60), z is the height determining the removals of particles, x is the distance from the left boundary, z_0 is the sample height (2.7m), a is the amplitude of the sine function and L is the wavelength of the sine function. In the simulation, the amplitude a=0.3m and the wavelength L=2m are assigned.

Parameters used in the calculations are shown in **Table 2**. Inter-particle friction is set for 0.51 except when circular particles are randomly sedimented in order to make disordered samples. In order to avoid dynamic effects, the coefficient of restitution and velocity of the loading plate are given a very small value. Spring constants for wall-particle contact are set to 10 times as large as those for particle-particle contact. As cylinder shaped particles are assumed, all the particles have unit in-plane depth.

(3) Simulation results

Figure 26 shows the settlement of the loading plate with increasing vertical stress on the plate. From the figure, in every case, there is a large settlement when the vertical stress is small (0-50kPa). After this initial settlement, the vertical stress starts to increase more rapidly in response to the settlement of the plate (50-250kPa). The stress-settlement relation becomes almost linear for a stress level over 250kPa where samples behave as a continuum material except for some intermittent stress releases seen for the samples consisting of circular particles. This result indicates that a foundation consisting of circular particles seems less stable than that consisting of rectangular particles when they are subject to vertical loading. Circular particles tend to rearrange more easily in response to a large vertical loading. There is no stress release for samples of rectangular particles. This is because rectangular particles are lock up easily and become very difficult to rearrange. Here, in this report, we identified three states according to the characteristics of the stress-settlement relations, i.e. the initial state (0-50kPa), the transition state (50-250kPa) and the final state (over 250kPa).

The stress-settlement relation is also affected by surface roughness. In the rough surface cases (CR, SR), there is a large settlement during both the initial and transition states simply because there is sufficient space for the particles near the surface to rearrange. However, the stress-settlement relations of both smooth and rough surface are almost linear and parallel to each other in the final state.

Table 2 Calculation conditions

Density	1650 (kg/m^3)
Normal spring constant	1.0*10^7 (N/m)
Tangential spring constant between particles	1.0*10^7 (N/m)
Normal spring constant between particle and wall	1.0*10^8 (N/m)
Tangential spring constant between particle and wall	1.0*10^8 (N/m)
Coefficient of restitution	0.01
Friction	0.51
Time step	0.00017078 (s)
Velocity of loading plate	0.01 (m/s)

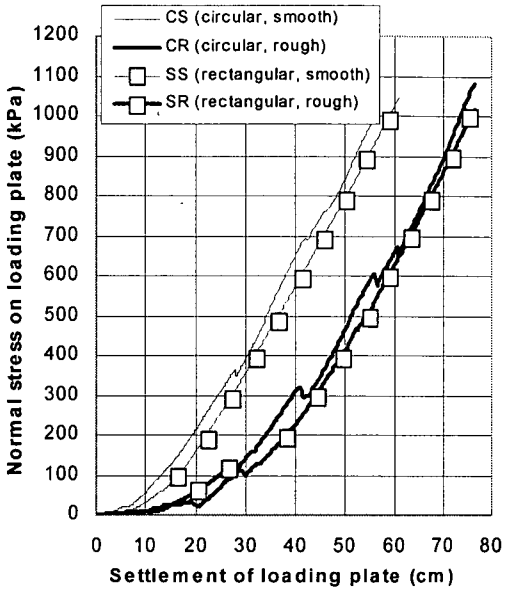

Figure 26 Relationship between settlement of loading plate and vertical stress on the plate

Figure 27 shows contact force distributions between particles for all cases. Each case includes snapshots of samples at the end of the initial and final states. In every case at the initial state, the number of contact points supporting the loading plate is small, however, there are some force chains which define force transmission paths developed even at this early state. In the transition state, although not shown here, the number of contact points on the plate increases and new force chains are created. In the final state, the surface roughness has diminished and most of particles near the surface are contacting the loading plate.

Comparing the two cases of a smooth surface, CS (circular particles, smooth) and SS (rectangular

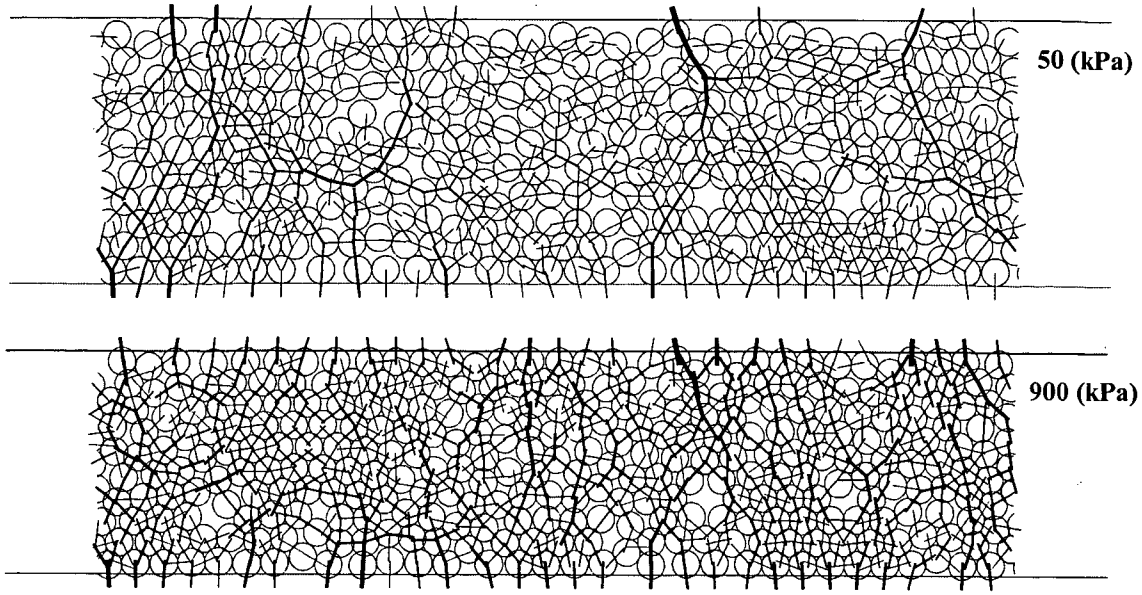

(a) Circular particle, Smooth surface (CS)

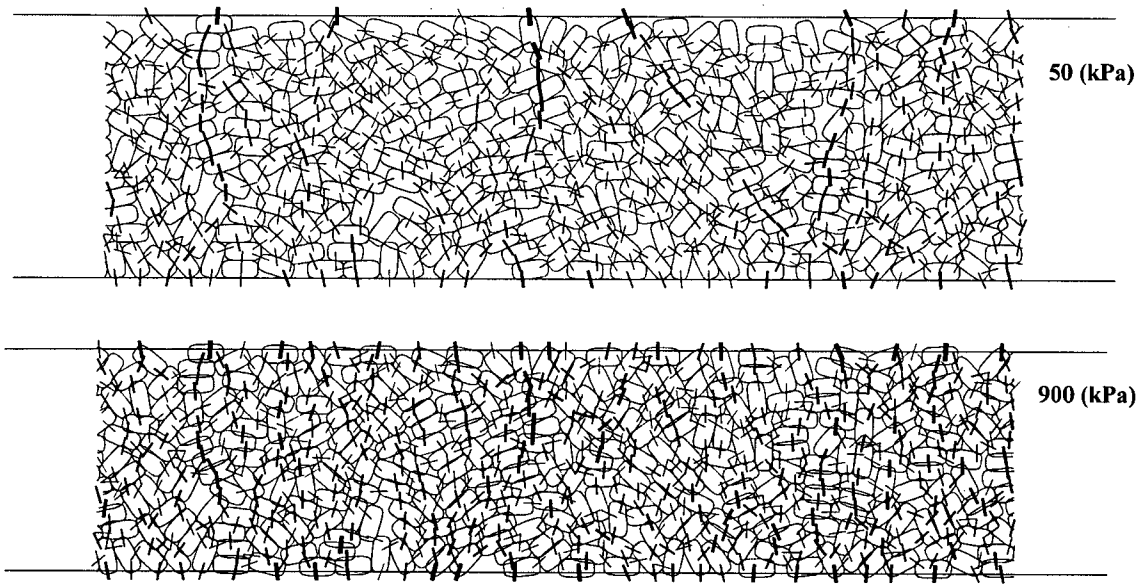

(b) Rectangular particle, Smooth surface (SS)

Figure 27(a) Contact force distributions between particles (Vertical stress = 50kPa and 900kPa)

particles, smooth), we ca see that there is a difference in the evolution of the force chains from the initial to the final states. For rectangular particles, the force chains formed in the initial state tend to endure through to the final state and continue to support the increasing load. On the other hand, for circular particles, initial force chains change continually through to the final state. This trend indicates that the force system within the system of rectangular particles is much more stable than that of a system of circular particles.

Figure 28 shows particle rotations between the initial unloaded state and after a loading of 50kPa vertical stress (initial state), and between 50kPa and 250kPa of the vertical stress for smooth roughness cases (CS, RS). The degree of the particle rotation is indicated by the darkness of the particle's color. For example, the maximum degree of particle rotation is shown as black and zero rotation is shown as white in each figure. As seen in the figure, significant particle rotations occur near the surface in both systems of circular and rectangular particles in the initial state and even in the

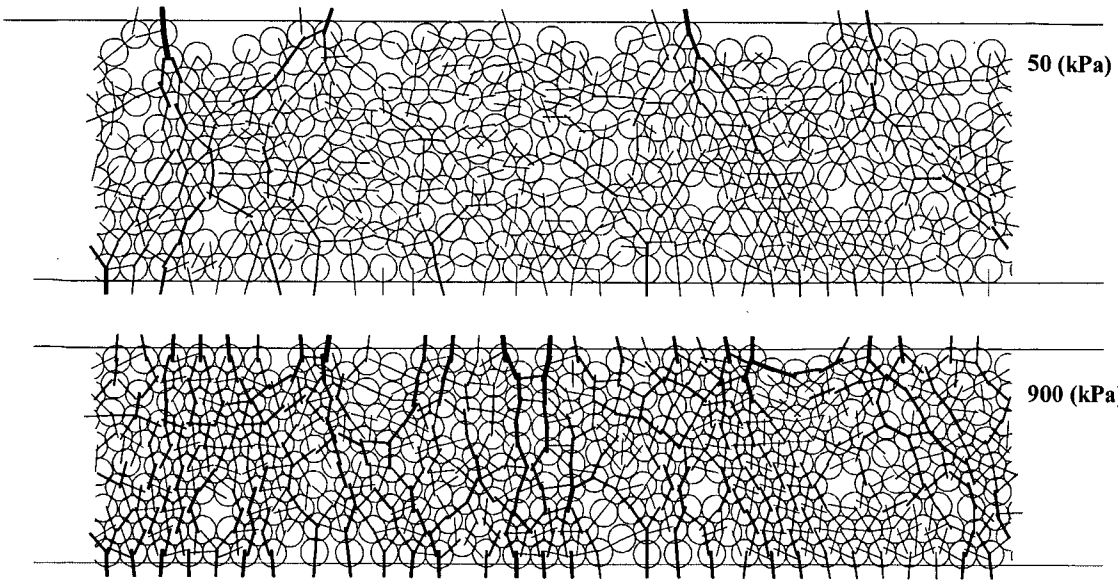

(c) Circular particle, Rough surface (CR)

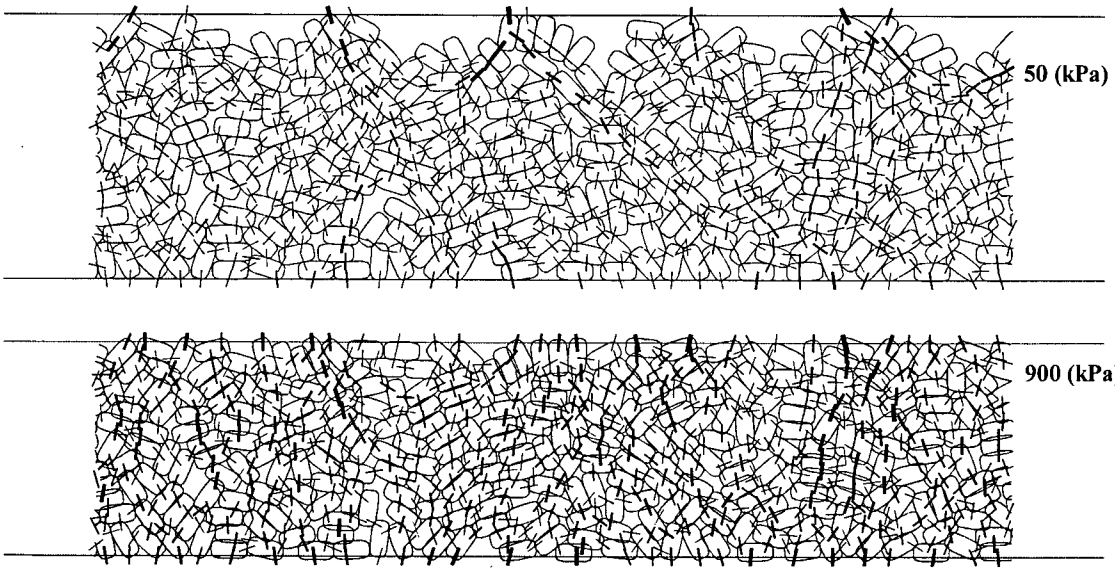

(d) Rectangular particle, Rough surface (SR)

Figure 27(b) Contact force distributions between particles (Vertical stress = 50kPa and 900kPa)

transition state. From a comparison between the systems of circular and rectangular particles, we find that the rotations of circular particles are much larger than those of the rectangular particles.

As shown in the figure, we find that particle rearrangement near the surface due to rotation is more significant than that of a particle near the bottom. In the figure, we also see that rectangular particles rearrange significantly less than circular particles. The particles near the surface seem to play a significant role in altering the force transmission paths. The degree of surface rearrangement of particles may also explain the occurrence of the sudden stress release predicted for a system of circular particles and its absence in a rectangular system of particles. A similar difference in the stability of the force systems can also be seen between the rough surface cases (CR and SR). However, more changes in the force chains occur in the rough

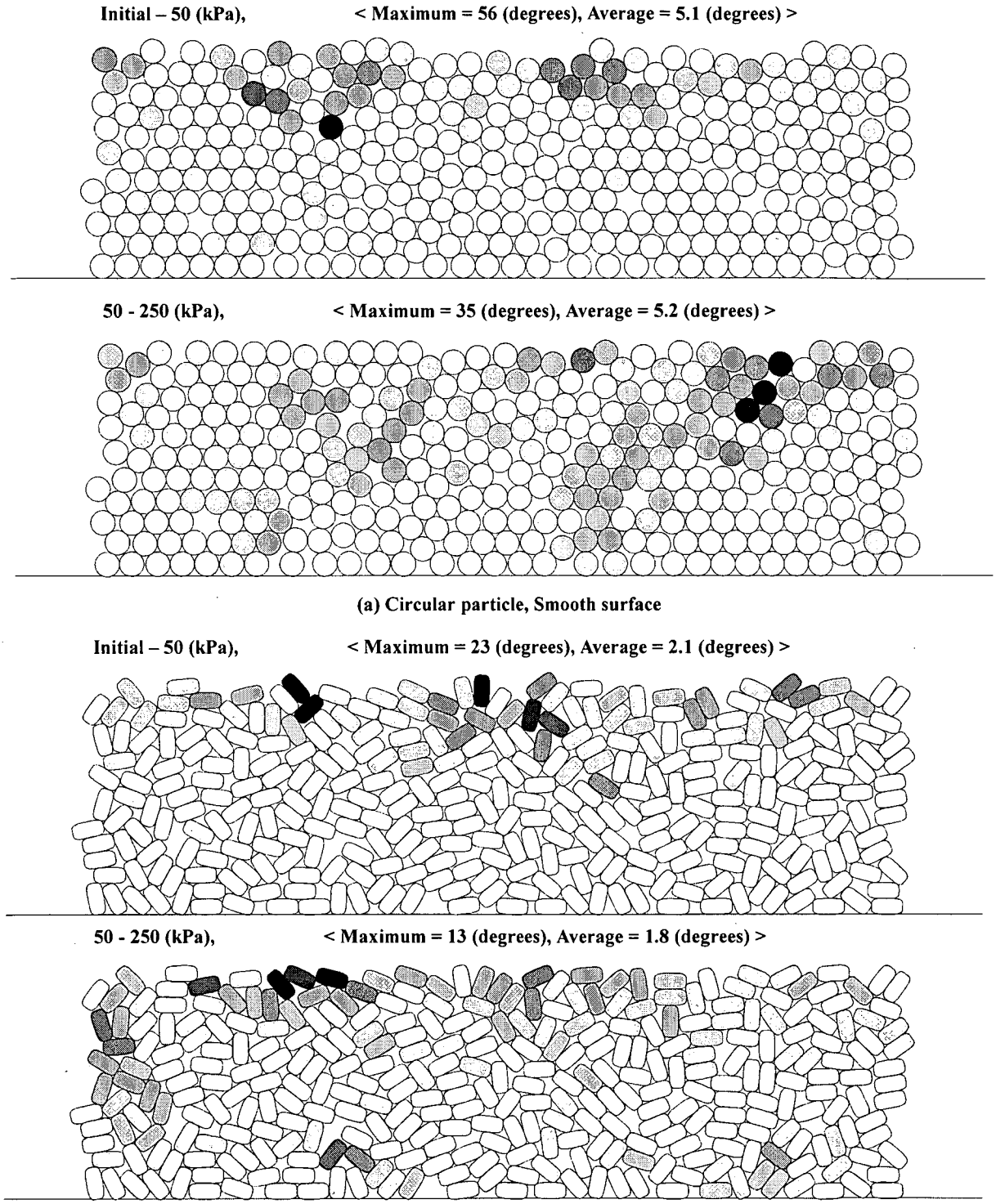

Figure 28 Particle rotations of Circular and Rectangular Particle Systems (CS, SS)

surface cases because there is more space available to accommodate particle movement near the surface.

Figure 29 shows how the number of contact points on the loading plate increases with the vertical stress. The number of contacts is normalized to define the ratio of the number of contact points on the loading plate to that of the bottom plate. Since the number of contacts on the bottom plate remains almost constant, we can compare the changes in the contact number for all the simulation cases on the same basis. In the figure, the

number increases quickly at the initial state. In the transition state, the number still increases, however, its rate of increase becomes smaller than that of the initial state. In the final state, the number increases even more slowly and approaches a maximum. In the present simulations, the effects of the particle shape on the number of contact points are inconclusive. On the other hand, the number of contacts for the rough surface cases is smaller than that for the smooth surface cases in the initial and transition states.

Figure 30 shows the percentage of the total load of 900kPa that is supported by the contacts formed in the initial, transition and final states respectively. For example, in the initial state, the first 40% of the contact points newly created is included. Similarly, the contacts formed between 40 and 70% and between 70 and 100%, define the transition and final state, respectively. Therefore, if every contact supported an equal amount of the vertical load, the percentage of the supporting load of each state should be 40% (initial), 30% (transition) and 30% (final). **Figure 30** illustrates that the contacts formed in the initial and transition states support over 70% of the total load. On the other hand, the contacts formed in the final state only support 20% or less of the total load. Therefore, we can conclude that the core chains of the force transmission system are most likely formed during the initial and transition states. This trend is clearly shown in the rectangular particle cases (SS, SR). The contacts formed in the initial state support more than 50% of the total load. On the other hand, the contacts formed in the final state support less than 15% of the total load. When a rubble rock foundation is constructed using non-spherical rocks and is subjected to the weight of a caisson, dominant persisting force chains may be created in the early state of the loading.

3.3 Uniaxial Compression Test Simulations using Three-dimensional Ellipsoidal DEM

We also conducted a similar uniaxial compression test using three-dimensional ellipsoidal particles. In this simulation, we focus our investigations on the characteristics of contact force distributions on a plate in a view of estimating bending moment acting on the bottom slab of a caisson.

Based on the simulation results, some preliminary observations and discussions are presented here on the contact force distributions of particulate systems. The effects of the surface roughness on the characteristics of the force distributions are also shown.

(1) Simulation method and calculation conditions

In the simulation, 1500 mono-size particles are inserted into a rectangular box (D=10m×W=10m)

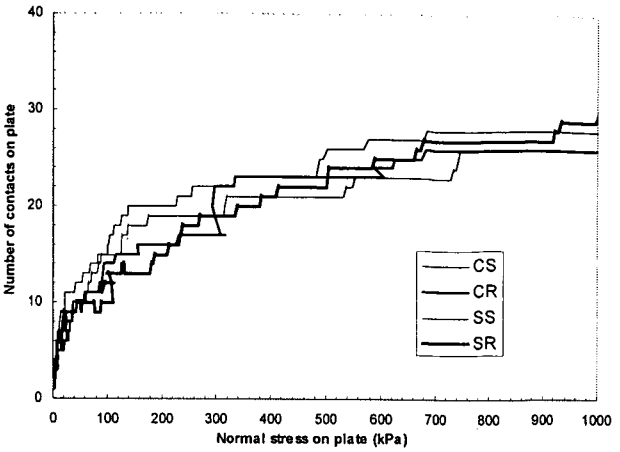

Figure 29 Evolution of normalized contact points on the loading plate with vertical stress

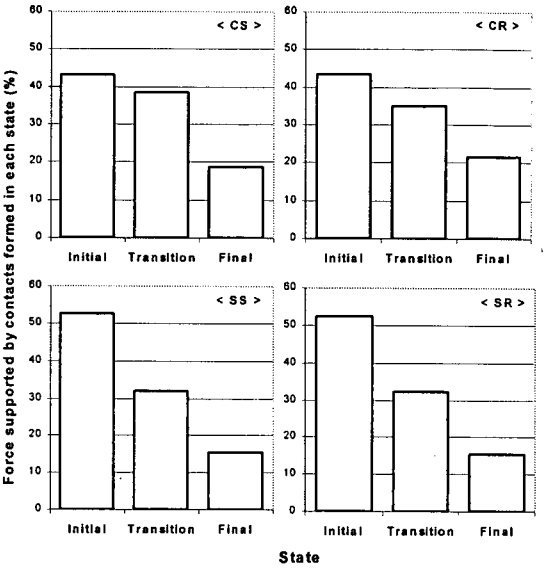

Figure 30 Percentage of the load supported by the contact points formed in each of initial, transition and final state (vertical stress = 900kPa)

Figure 31 Simulation model

where all sides are periodic boundaries to minimize the boundary effects as shown in **Figure 31**. The sample is then allowed to settle and reach the static equilibrium condition. After the settlement, particles, whose centers are located at higher than 2.0m (31 particles), were removed to obtain flatter surface of the sample. After further settlement, a loading plate is placed at the maximum height of the sample and is lowered at a

constant velocity in the vertical direction. The velocity is chosen small enough to maintain quasi-static behavior of the particles. During calculations, the total vertical load acting on the plate and settlement of the plate are recorded. Contact conditions such as the number of contact points, locations of the contacts, force amplitudes of the contacts between the loading plate and particles beneath the plate are monitored as well. Movements and rotations of all the particles and contact forces between particles are also recorded.

A rubble rock shape was modeled by an ellipsoid with semi axes ratios of (1:0.7:0.49). These ratios were determined based on the shape measurement results of actual rubble rocks, which are used in ports of Japan (Shoji 1983). In this simulation, these semi axis length are given as 37.1, 26.0, 18.2cm respectively. The mass of a single particle is about 191kg. Inter-particle and wall-particle friction coefficients are set to the same value of 0.6. In order to avoid dynamic effects, the velocity of the loading plate is given a very small value (2cm/s). Note, that the Hertz contact force law was applied in these analyses. The Young's modulus and Poisson's ratio are given as 70GPa and 0.2 respectively for both of the particles and the loading plate. The time step was defined as 6.86×10^{-6} second during the compression process.

(2) Simulation results

Figure 32 shows the evolution of the vertical stress on the loading plate with increasing vertical settlement of the plate. From the figure, there is a large settlement when the vertical stress is small (0-100kPa). After this initial settlement, the vertical stress starts to increase more rapidly in response to the settlement of the plate (100-400kPa). The stress-settlement relation becomes almost linear for the stress levels over 400kPa where rubble rock samples behave as a continuum material. Here, in this report, we identified three states according to the characteristics of the stress-settlement relations, i.e. the initial state (0-100kPa), the transitional state (100-400kPa) and the final state (over 400kPa).

Figure 33 shows the evolution of the number of contact points on the loading plate with increasing vertical stress on the loading plate. The increase in the number of contacts seems to be related to the stress-settlement behavior. The number of contacts increases quickly in the initial state. In the transitional state, the number of contacts still increases, however, its rate of increase versus the vertical stress becomes smaller than that during the initial state. In the final state, the rate of increase becomes even smaller still. On the other hand, the number of contacts on the bottom plate remains almost constant at about 257 during compression since the particles generated in the box are allowed to settle freely to the bottom plate and it made

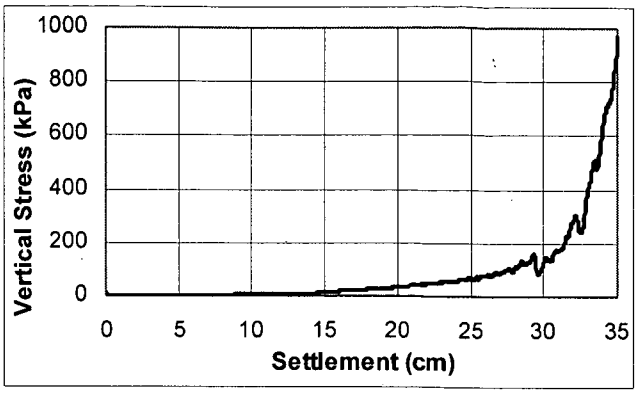

Figure 32 Stress-Settlement relations of loading plate

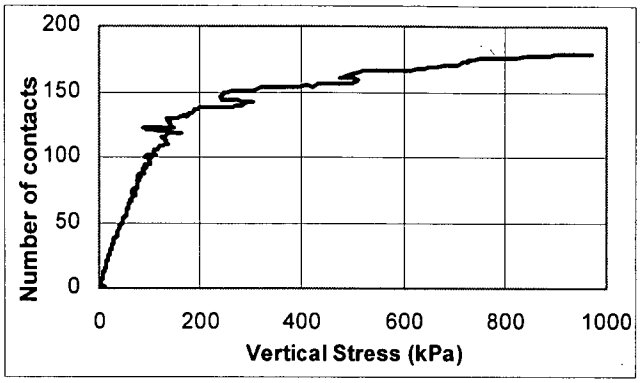

Figure 33 Evolution of number of contact points

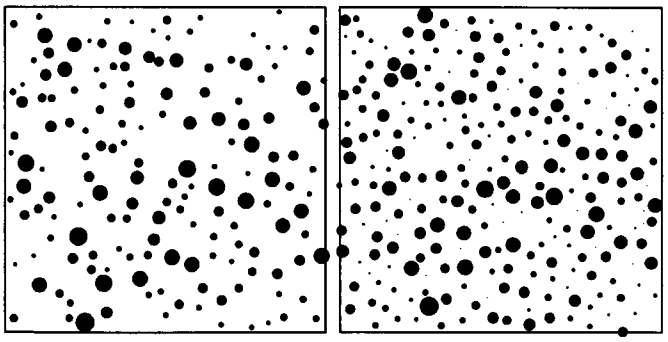

Figure 34 Contact force distributions
(Left: a) Loading plate, Right: b) Bottom plate)

more particles have contacts with the bottom plate. Therefore, the top surface of the specimen may be identified as a "smooth surface" and the bottom surface may be identified as a "rough surface" in this simulation.

Figure 34(a) shows the contact force distributions between particles and the loading plate when the vertical stress is 400kPa. The area of each circle represents the force amplitude of each contact point on the plate. As shown in the figure, the contact force has a wide range of amplitude even in the final state where the particles are compressed to a high vertical stress. **Figure 34(b)** shows the contact forces acting on the bottom plate. Though the number of contact points on

the bottom plate is much greater than those acting on the loading plate, the contact force amplitudes also have a wide variation. It is also interesting to note that primary force systems that support a large portion of the total load are similar for both a "smooth surface" (top surface) and a "rough surface" (bottom surface).

Figure 35 shows the probability density distributions of normalized contact force amplitude f, on both the loading and the bottom plates (shown by bars). The normalized contact force is defined by dividing each contact force by the average contact force on the plate at each vertical stress level. Each distribution was obtained by using 10 snapshots of contact forces between 400kPa and 600kPa of the vertical stress. As shown in the figure, we find that there is a difference in the shape of distribution at $f < 1.0$ between the loading and bottom plates. We also see that the amplitude of contact force has a wide variation. From the figure we can notice that most of the contacts generate relatively small contact forces on both the plates.

In the figure, we also plotted two sets of probability density functions. The thick line was obtained from a series of uniaxial compression tests using glass bead packs by Mueth et al. (1998). The function is represented as follows:

$$P(f) = a \cdot (1 - b \cdot e^{-f^2}) \cdot e^{-\beta f}, \qquad (61)$$

where f is normalized contact force. The three parameters in the function are given as a=3, b=0.75 and β=1.5 respectively.

The dotted line is a theoretical model proposed by Liu et al. (1995) and Coppersmith et al. (1996), which has been named as " q-model". The q-model is a scalar model which takes the normal component of force determined by the weights of elements located in an ordered lattice. For further details, see the references above. This function is represented as follows:

$$P(f) = \frac{N^N}{(N-1)!} f^{N-1} e^{Nf} \qquad (62)$$

where N is the number of underlying neighbors in the lattice. In this work, N=3 was used.

There is an exponential decay at large f>1.0 in both the functions (61) and (62). Furthermore, aother numerical simulation (Radjai, 1996) and experimental results (Baxter 1997, Lovoll 1999) also have shown the same exponential decay. Therefore, this exponential decay seems to be one of the characteristics of a force distribution within an assembly of particulate media. On the other hand, however, there is no consensus on the shape of the distribution for small forces $f < 1.0$. Our simulation results show that the distribution on the loading plate is a good fit to the function (62) predicted by the q-model, and the distribution on the bottom plate

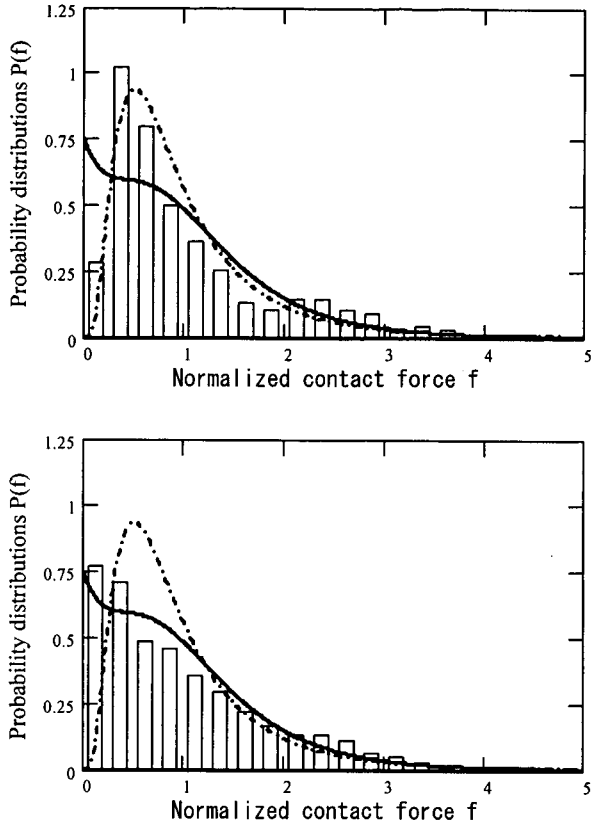

Figure 35 Probability density distributions of normalized contact force

is a good fit to the function (61) that was obtained by experiment.

Our final goal is an estimation of the bending moment of the bottom plate of a caisson, which is subjected to loading by distinct concentrated forces from the rubble rocks. By using both the probability density function of contact force amplitude and the spatial distribution of contact points on the plate, we are able to estimate the moment in a statistical manner through Monte Carlo simulations (Miyata et al. 1999). **Figure 36** shows a flow diagram for estimating the bending moment due to arbitrary contact forces by a statistical way. From the point of view regarding the estimation of moment, we are able to say that relatively larger contact forces will dominate the fluctuation of the maximum bending moment of the plate. On the other hand, the effect of small contact forces, which are located homogeneously in space, on the moment fluctuation is most likely to be small.

Figure 37 shows a probability density distribution that represents the percentage of the total load within

each class of the normalized force f. The thick line and dotted line show the distributions for the loading plate ("rough surface") and the bottom plate ("smooth surface"), respectively. As shown in the figure, small contact forces ($f < 0.5$) support a small portion of the total load, while medium ($0.5 < f < 2.0$) and large contact forces ($f > 2.0$) support a significantly larger portion of the total load. The fluctuation of the moment will be strongly affected by this load support probability distribution rather than the contact force distribution. Accordingly, the above results indicate that the shape of the distribution function of contact force for $f > 0.5$ is of considerable importance.

4 Concluding Remarks

(1) The current report describes the general theory of the DEM and the mathematical development of a two-dimensional superquadric DEM and a three-dimensional ellipsoidal DEM for analyzing systems of general shaped rigid particles.

(2) We investigate the force support systems of particulate media such as a rubble rock foundation by using the two DEMs. In the DEM simulations, rubble rocks are modeled by smooth frictional particles. The rocks are then subject to a vertical loading of the weight of a caisson. DEM simulations performed in this report consisted of: a) uniaxial compression tests of particulate media using the two-dimensional superquadric DEM, and b) similar tests using the three-dimensional ellipsoidal DEM. From these DEM simulations, the following remarks were made.

a) Uniaxial Compression Test Simulations using two-dimensional superquadric DEM

Based on the simulation results for the uniaxial compression test using the superquadric DEM, it has been shown that both surface roughness and particle shape significantly affect the stress-settlement relation of a particle assembly. A rough surface initially leads to a large settlement in the compression process. Systems of circular particles exhibit some intermittent stress releases during the settlement while systems of rectangular particles tend to form rigid stable force chains that persist throughout the compressive loading. The simulation results have also shown that the force chains developed in the earlier stage of compaction process, supports a larger proportion of the total load. This trend is more apparent for the systems of rectangular particles than for those of circular particles. In the evolution of the force system, the differences between circular and rectangular particles seem to cause the differences in the local rearrangement of particles near the surface of the particle assemblies.

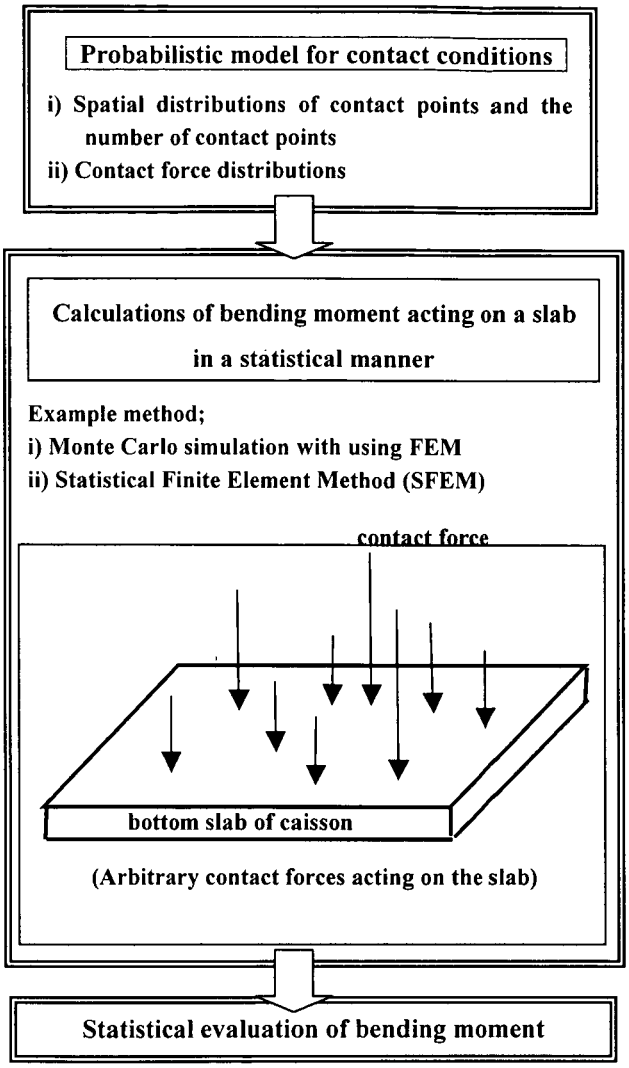

Figure 36 Flow diagram for statistical evaluation of bending moment acting on a slab due to arbitrary contact forces

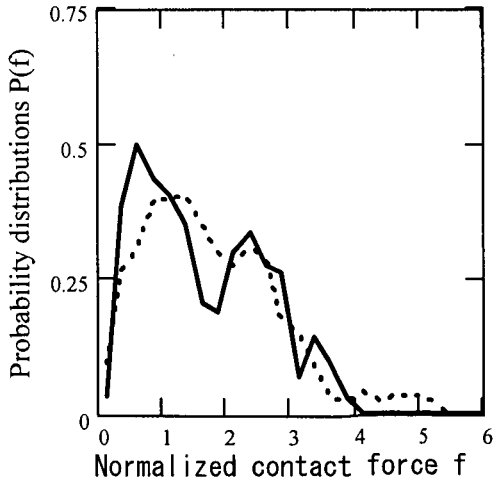

Figure 37 Probability density distributions of load support ratio

b) Uniaxial Compression Test Simulations using Three-dimensional Ellipsoidal DEM

Based on the simulation results for the uniaxial compression test using the three-dimensional ellipsoidal DEM, it has been shown that stress-settlement relations of an assembly of particulate media, which is subjected to vertical loading, is related to the evolution of the number of supporting contact points. The number of contact points on the loading plate increases quickly during an initial large settlement of the sample. After the initial settlement, its rate of increase becomes much slower and the stress-settlement relation becomes almost linear as in a continuum material.

The simulation results have also shown that the contact force amplitudes on the loading plate and the bottom plate, which may be identified as a "rough surface" and a "smooth surface" in this simulation respectively, have a wide range of distribution. This discrete and inhomogeneous force support system of particulate media is apparently very different from the linearly distributed reaction force between a rubble rock foundation and a bottom slab of a caisson, which is assumed in the present design code. Though more studies are needed to clarify the differences in the force support system between "smooth surface" and "rough surface" of a rubble rock foundation, the simulation results indicate that principal force support systems that support a large portion of the total load are similar for both a "smooth surface" and a "rough surface". This result suggests that we may be able to employ a rougher rock rubble surface foundation instead of the smooth rock rubble surface foundation used at present.

Characteristics of the probability density distributions of normalized contact force f, which is defined by dividing each contact force by the average contact force on the plate at each vertical stress level, were investigated for both loading and bottom plates. The results have shown that the amplitude of normalized contact force f has a wide variation and the shape of the distribution for large contact forces $f > 1.0$ decays exponentially as the normalized contact force f increases. This work agreed with other studies performed by DEM simulations, theoretical investigations and experiments which also showed the presence of this exponential decay for larger contact forces $f > 1.0$. Accordingly, this exponential decay seems to be one of the characteristics of a force distribution within an assembly of particulate media. On the other hand, there is no consensus on the shape of the distributions for small contact forces $f < 1.0$. However, the effects of the distributions shape near $f = 0$ on the fluctuations of bending moment on the bottom plate of a caisson is considered to be small. Therefore, with respect to the practical use of these probability distributions, we should consider the load support distributions rather than contact force amplitudes distributions.

(3) The present work using the DEM highlights the applicability of DEM to the analysis of compaction problems of particulate media and more particularly to the port engineering problems. This report clearly shows that the DEM can predict detailed particulate level information, which is essential in the development of new design guidelines for the bottom slab of a caisson. (*Received on February* 14,2002)

Acknowledgements

The authors kindly acknowledge support and advice from Dr. David Wu and all the other members of the Particulate Science and Technology Group (PSTG) at Colorado School of Mines. The first author also would like to express his sincere acknowledgement to the Study Fellowship Program through the Science and Technology Agency (STA) of Japan and all the members of the Structural Dynamics Laboratory at Port and Harbour Research Institute (Port and Airport Research Institute at present).

References

Alder, B.J. and Wainwright, T.E. (1956): Statistical Mechanical Theory of Transport Properties, *Proceedings of the International Union of Pure and Applied Physics*, Brussels, 1956 (unpublished).

Barr, A.H. (1981): Superquadrics and Angle-Preserving Transformations, IEEE, *Computer Graphics and Applications*, 1, pp.1-20.

Baxter, G.W. (1998): Stress Distributions in a Two Dimensional Granular Material, in Behringer & Jenkins (eds), *Powders & Grains 97*, 345-348. Rotterdam: Balkema.

Boresi, A. P. and Sidebottom, O.M. (1984): Advanced Mechanics of Materials, 4th ed., Wiley, NY.

Brent, R.P. (1971): An Algorithm with Guaranteed Convergence for Finding a Zero of a Function, *The Computer Journal*, 14, 422-425.

Coppersmith, S.N., Liu, C.-h. Majumdar S., Narayan, O. & Witten T.A. (1996): Model of Force Fluctuations in Bead Packs, *Physical Review E* 53: 4673-4685.

Cundall, P.A. (1971): A computer Model for Simulating Progressive Large Scale Movements in Blocky Rock Systems, *Proc. of the Symposium of the International Society for Rock Mechanics* (Nancy, France), Vol. 1, Paper No. II-8.

Cundall, P.A. & Strack, O.D.L (1979a): The Distinct Element Method as a Tool for Research in Granular Media, Part II, Report to NSF, Dept. of Civil and Mineral Eng., Univ. of Minnrsota, MN, USA.

Cundall, P.A. and Strack, O.D.L (1979b): A Discrete Numerical Model for Granular Assemblies, *Geotechnique*, London, England, 29 (1), pp.47-65.

Cundall, P.A. (1980): UDEC – A Generalized Distinct Element Program for Modeling Jointed Rock," ReportPCAR-1-80, Peter Cundall Associates Report, European Research Office, U.S. Army, Contract DAJA37-79-C-0548.

Cundall, P.A. (1987): Distinct Element Models of Rock and Soil Structure, in *Analytical and Computational Methods in Engineering Rock Mechanics*, Ch. 4, pp.129-163, E.T. Brown, Ed. London: Allen & Unwin.

Dobry, R. and Ng, T.-T. (1989): Dicsrete Modeling of Stress-Strain Behavior of Granular Media at Small and Large Strains, *in Proceedings of the 1st U.S. Conference on Discrete Element Methods*, Mustoe, G.G.W., Henriksen, M. and Huttelmaier, H.P., eds., Golden, CO., USA.

Mindlin, R.D. and Deresiewicz, H. (1953): Elastic spheres in contact under varying oblique forces. J. Appl. Mech. 20, ASME: 327-344

Hertz, H. (1882): Ueber die Beruhrungfester Elastischer Korper, *Journal Renie Angew. Math.*, 92, pp.156-171.

Hocking, G., (1978): Analysis of Toppling-Sliding Mechanisms for Rock Slopes, *19th US Rock Mechanics Symposium*, Reno, Nevada USA.

Hocking, G., Mustoe, G.G.W. and Williams, J.R. (1985): Validation of the CICE Discrete Element Code for Ice Ride-up and Ice Ridge Cone Interaction, *Proc. ASCE Specialty Conference*, ARCTIC '85, San Francisco.

Hocking, G., Mustoe, G.G.W., and Williams, J.R., (1987): Dynamic Analysis for Generalized Three-Dimensional Contact and Fracturing of Multiple Bodies, *Proc. NUMETA Conf., Swansea*, U.K., A.A. Balkema, Publishing Co., Rotterdam.

Hocking, G., (1992): The Discrete Element Method of Analysis of Fragmentation of Discontinua, *Journal of Engineering Computations*, Vol. 9, pp145-155.

Hocking, G., (1993): Collision Impact of a Ship with Multi-Year Sea Ice, *Proceedings of the 2nd International Conference on Discrete Element Methods*, pp369-378, MIT Press, Boston, MA.,USA.

Itasca Consulting Group, Inc. (1999): PFC2D and PFC3D Particle Flow Code Computer Documentation Manuals, Minneapolis, MN., USA.

Iwashita, K. and Oda, M. (1998): Rotational Resistance at Contacts in the Simulation of Shear Band Development by DEM, *J. Eng. Mech. Div.*, 124 (3), ASCE: pp285-292.

Technical Standards for Port and Harbour Facilities in Japan (1983): Bureau of Ports and Habours and Port and Harbour Research Institute, Ministry of Transport ed., OCDI (The Overseas Coastal Area Development Institute of Japan): Tokyo, Japan.

Johnson, K. L. (1985): Contact Mechanics, Cambridge: Cambridge Univ. Press.

Lin, X. (1995): Numerical Study of Granular Soil Behavior using Random Arrays of Elastic Ellipsoids, Ph.D., thesis, University of New Mexico, USA.

Lin, X., and Nakagawa, M. and Mustoe, G.G.W. (1996): Simulations on Hopper Flow of Elongated Particles, *Proceedings of the 5th World Congress of Chemical Engineering, Sponsored by the Institute of Chemical Engineers*, San Diego.

Lin, X and Ng, T-T. (1995): Contact Detection Algorithms for Three-Dimensional Ellipsoids in Dsicrete Element modeling, *Int. J. Numer. Anal. Methos Geomech. 19, pp.653-659.*

Lin, X and Ng, T-T. (1997): A Three-dimensional Discrete Element Model using Arrays of Ellipsoids, *Geotechnique* 47, pp.319-329.

Lipschutz, M. M. (1969): Theory and Problems of Differential Geometry, Schaum's Outline Series, McGraw-Hill.

Liu, C.-h., Nagel, S.R., Shecter, D. and Coppersmith S. (1995): Force Fluctuations in Bead Packs, *Science* 269: 513-515.

Lovoll,G., Maloy, K.J. and Flekkoy, E.G. (1999): Force Measurements on Static Materials, *Physical Review E* 60: 5872-5878.

Mindlin, R. D. (1949): Compliance of elastic bodies in contact, *J. Appl. Mech.*, Sept., pp.259-268.

Mindlin, R. D. and Deresiewicz, H. (1953): Elastic Spheres in Contact Under Oblique Forces, *Trans. ASME, J. Appl. Mech.*, 20, pp.327-344.

Miyata, M., Sugano, T., Nagao, T., Shinohara, K. and Kondoh, T. (1999): The Effect of Surface Configuration of Rubble Mounds on the Stress on the Bottom Slab of Caisson, *Technical Note of the Port and Harbour Research Institute (PHRI)*, No.945. (in Japanese)

Miyata, M., Nakagawa, M. and Mustoe, G.G.W. (2000): Design Considerations of Rubble Rock Foundations based on a Discrete Superquadric Particle Simulation Method, *Finite Elements: Techniques and Developments (Proc. of the 2nd Int. Conf. on Engineering Computational Technology*, Topping, B.H.V. ed., Leuven, Belgium), pp213-218.

Mueth, D.M., Jaeger, H.M. and Nagel, S.R. (1998): Force Distribution in a Granular Medium, *Physical Review E* **57**: 3164-3169.

Mustoe G.G.W. (1992): A Generalized Formulation of The Discrete Element Method, *Engineering Computations*, Vol. 9, No. 2, pp181-190.

Mustoe, G.G.W and DePoorter, G. (1993): A Numerical Model for the Mechanical Behavior of Part iculate Media Containing Non-Circular Shaped Particles, *Powders and Grains 93* (C. Thornton, editor), pp.421-427, Balkema.

Mustoe, G.G.W. and Griffiths, D.V. (1998): An Equivalent Continuum Model using the Discrete Element Method (DEM), *ASCE Specialty Conference - Engineering Mechanics*, San Diego.

Mustoe, G.G.W. & Miyata, M. (2001): Material Flow Analysis of Non-Circular Shaped Granular Media using Discrete Element Methods, *ASCE Journal of Engineering Mechanics*, Vol.127, No.10, pp1017-1026.

Mustoe, G.G.W., Miyata, M. and Nakagawa, M. (2000 a): Discrete Element Methods for Mechanical Analysis of Systems of General Shaped Bodies, *Finite Elements: Techniques and Developments (Proc. of the 5th Int. Conf. on Computational Structures Technology*, Topping, B.H.V. ed., Leuven, Belgium), pp219-224.

Mustoe, G.G.W., Miyata, M. and Nakagawa, M. (2000 b): A Numerical and Experimental Study of the Performance and Safety Issues for Ore Pass Systems (RP-5), WMRC Annual Progress Project Report 1999-2000, October.

Nakagawa, M., Mustoe, G.G.W., Lin, X., Iwamoto, N. (1999): Simulation of Particle Compaction for Conductive Adhesives Using Discrete Element Modeling, *Proceeding of 49th Electronics Components and Technology Conference*, June.

Ng, T.-T. and Dobry, R. (1992): A Non-linear Numerical Model for Soil Mechanics, *Int. J. Numer. and Analytical Methods in Geomech.*, 16, pp.247-263.

Ng, T-T and Lin, X. (1993): Numerical Simulation of Naturally Deposited Granular Soil with Ellipsoidal Elements, *Proc. of the 2nd Int. Conf. on Discrete Element Methods* (Williams, J. R. and Mustoe, G.W. G., eds.), pp.557-568, MIT Press, Boston, MA., USA.

Ng, T.-T. (1994): Numerical Simulation of Granular Soil Using Elliptical Particles, *Computers and Geotechnics*, 16, pp.153-169.

Ng, T.-T. and Dobry, R. (1994): A Non-linear Numerical Model for Soil Mechanics, *J. Geotech. Engrg.*, ASCE, 120(2), pp388-403.

Proceedings of the 1st U.S. Conference on Discrete Element Methods. (1989): Mustoe, G.G.W., Henriksen, M. and Huttelmaier, H.P., eds., Golden, CO., USA, Golden: CSM press.

Proceedings of the 2nd International Conference on Discrete Element Methods. (1993): Williams, J. R. and Mustoe, G.G.W., eds., MIT Press, Boston, MA., USA, Golden: CSM press.

Radjia, F., Jean, M., Moreau, J-J. and Roux, S., N. (1996): Force Distributions in Dense Two-Dimensinal Granular Systems, *Physical Review Let.* 77, pp274-277.

Rothenburg, L and Bathurst, R. J. (1991): Numerical Simulation of Idealized Granular Assemblies with Plane Elliptical Particles, *Computers and Geotechnics*, 11, pp.315 – 329.

Sawada, S. and Pradham, T. B. S. (1994): Analysis of Anisotropy and Particle Shape by Distinct Element Method", *Computer Methods and Advantages in Geomechanics*, Siriwardane and Zaman, eds., Balkema, Rotterdam, The Netherlands, pp.665-670.

Seridi, A. and Dobry, R., (1984): An Incremental Elast9c-Plastic Model for the Force-Displacement Relation at the Contact Between Elastic Spheres, Research Report, Department of Civil Engineering, Rensselaer Polytechnic Institute, Troy, NY, USA.

Seville, J. P.K., Fan, L.S., Horio, M., Lieberman, A., Clift, R., Williams, J.C. and Thornton, C. eds., (2000): Numerical Simulations of Discrete Particle Systems, *Special Issue of J. Powder Technology*, Vol. 109.

Shoji, Y. (1983): Study on Shearing Properties of Rubbles with Large Scale Triaxial Compression, *Report of the Port and Harbour Research Institute (PHRI)*, Vol. 22, No.4. (in Japanese)

Thornton, C. and Randall (1988): Applications of Theoretical Mechanics to Solid Particle System Simulations, in *Mechanics of Granular Materials*, Sateke and Jenkins editors., Elsevier Science Publ., Amsterdam, Netherlands, pp.133-142.

Ting, J. and Corkum, B. T. (1988): Strength Behavior of Granular Materials using Discrete Numerical Modeling, *Numerical Methods in Geomechanics*, Innsbruck, pp.305-310.

Ting, J. M., Khwaja, M., Meachum, L. R. and Rowell, J. D. (1993): An Ellipse-Based Discrete Element Model for Granular Materials, *Int. J. for Numerical and Analytical Methods in Geomechanics*, Vol 17, pp.603-623.

Tsuchikura, T. Fukusawa, T. and Murakami, Y. (1995): Application of the Granular Element Method to the Stability Analysis on the Models of Rock Slopes, *Journal of Geotechnical Engineering* (Japan Society of Civil Engineers), No. 523/III-32, pp.125-132. (in Japanese)

Walton, O.R., Braun, R.L. (1993): Simulation of Rotary-drum and Responce Tests for Frictional Spheres and Rigid Sphere Clusters, DOE/NSF Workshop on Flow of Particulates and Fluids, pp.1-17.

Williams JR, Pentland (1989): A. Superquadrics and Modal Dynamics for Discrete Elements in Concurrent Design, In: Mustoe GGW, Henriksen M,

Huttelmaier HP, editors. *Proc. of the 1st U.S. Conf. on Discrete Element Methods*. Golden: CSM press, 1989.

Yamane, K., Nakagawa, M., Altobeli, S.A., Tanaka, T. and Tsuji, Y. (1998): Steady Particulate Flows in a Horizontal Rotating Cylinder, *Physics of Fluids*, American Society of Physics, Vol 10, No. 6, pp.1419-1427.